Research Square

Preprints are preliminary reports that have not undergone peer review.
They should not be considered conclusive, used to inform clinical practice,
or referenced by the media as validated information.

Natural Sesquiterpenoids from Laggera pterodonta as bioactive Acetylcholinesterase Inhibitors: Insights from DFT, Molecular Docking, and ADMET Profiling

Hamza Iftikhar
Ghazi University
Muhammad Mohsin Ejaz
Ghazi University
K. S. Al-Namshah
Imam Mohammad Ibn Saud Islamic University (IMSIU)
Saira Khan
Ghazi University
Sadaf Ashraf
University of Balochistan
Nazia Meer
University of Balochistan
Musarat Riaz
Sardar Bahadur Khan Women's University
Muhammad Saleem
msaleem@gudgk.edu.pk

Ghazi University

Research Article

Keywords: Alzheimer's disease, natural extracts, computational analysis, Molecular docking and ADMET

Posted Date: October 20th, 2026

DOI: https://doi.org/10.21203/rs.3.rs-11218173/v1

License: This work is licensed under a Creative Commons Attribution 4.0 International License.
Read Full License

Additional Declarations: No competing interests reported.

Natural Sesquiterpenoids from Laggera pterodonta as bioactive Acetylcholinesterase Inhibitors: Insights from DFT, Molecular Docking, and ADMET Profiling

Hamza Iftikhar[a], Muhammad Mohsin Ejaz[a], K.S. Al-Namshah[b], Saira Khan[a], Sadaf Ashraf[c] ,Nazia Meer [c], Musarat Riaz [d], Muhammad Saleem[*a]

[a] *Department of Chemistry, Faculty of Science, Ghazi University, Dera Ghazi Khan, 32200, Pakistan*

[b] *Department of Chemistry, College of Science, Imam Mohammad Ibn Saud Islamic University (IMSIU), Riyadh, 11623, Saudi Arabia.*

[c] *Department of Chemistry, University of Balochistan, Quetta, Balochistan, 83700, Pakistan*

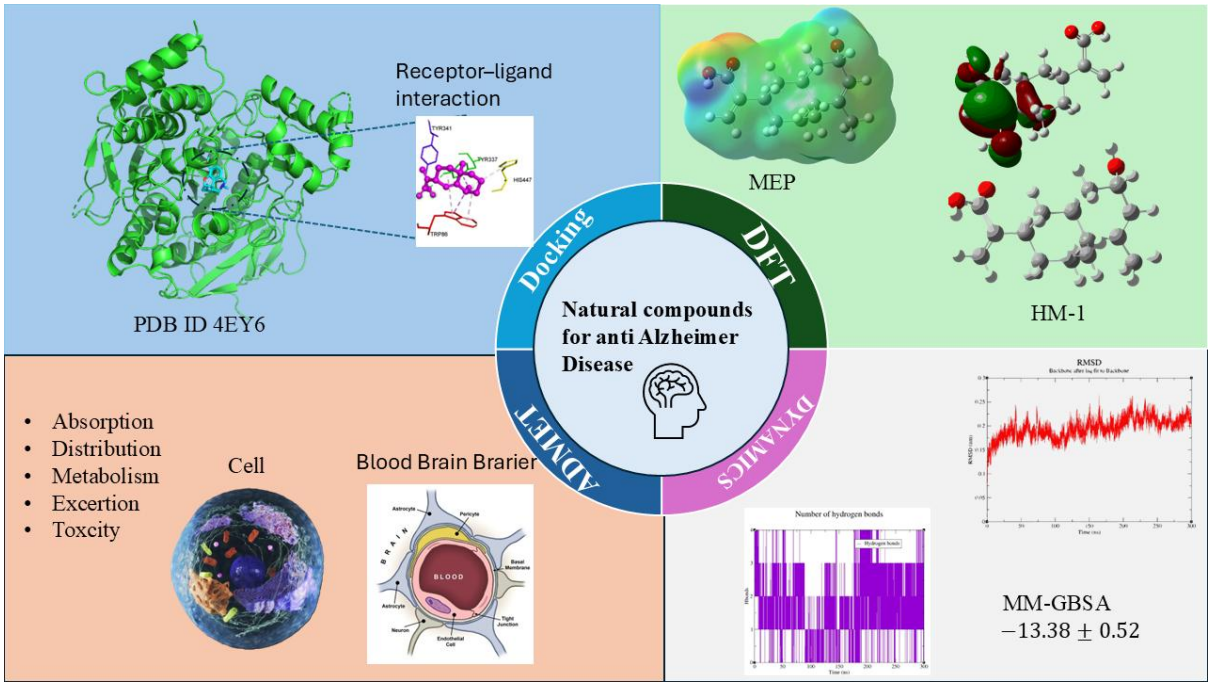
[d] *Department of Chemistry, Sardar Bahadur Khan Women's University, Quetta, Balochistan, 83700, Pakistan*

*Correspondance: msaleem@gudgk.edu.pk ; hod.chem@gudgk.edu.pk.

Abstract

Alzheimer's disease continues to be one of the major critical neurodegenerative ailments of the modern era, with acetylcholinesterase (AChE) inhibition standing as a foundational therapeutic strategy. Natural products continue to provide a rich, sustainable source of structurally diverse bioactive scaffolds that offer sustainable options in the search for new treatments. In this study, five **(05)** naturally occurring sesquiterpenoids isolated from a single botanical source, *Laggera pterodonta,* designated as **HM-1** to **HM-5**, were investigated as potential AChE-targeting candidates through a unified in silico framework, evaluated against the clinically established drug galantamine. Density functional theory (DFT) at the B3LYP/6-311G (d, p) level elucidated the electronic structures of these compounds, including frontier molecular orbitals, density of states, global reactivity descriptors, molecular electrostatic potential, non-covalent interaction topology, and electron localization, while time-dependent DFT further identified their optical signatures Molecular docking showed that all five natural compounds interacted with the AChE active site with binding affinities closer to galantamine; **HM-1** had the highest binding value of all **(-8.6 kcal/mol**), inducing stable interactions via hydrogen bonding and π-mediated contacts inside the catalytic cavity of the enzyme. A 300 ns molecular dynamics simulation of the AChE–**HM-1** complex further supported its conformational stability, with stable backbone RMSD and radius of gyration, persistent hydrogen-bonding interactions, and localized residue flexibility. MM/GBSA analysis yielded a binding enthalpy of **−14.37 ± 0.38 kcal/mol**, with van der Waals interactions providing the major favourable energetic contribution, further supporting the stable association of **HM-1** with the AChE active site. Notably, ADMET profiling showed that while galantamine retained a slight edge in intestinal absorption and blood-brain barrier permeability, two of the five natural compounds (**HM-1** and **HM-5**) achieved comparable brain penetration, and all five candidates exhibited a safer toxicity profile relative to the reference drug, especially showing reduced neurotoxic and immunotoxin potential.

Keywords: Alzheimer's disease, natural extracts, computational analysis, Molecular docking and ADMET.



Graphical Abstract.

1. Introduction

Alzheimer's disease (AD) is a rapidly increasing neurodegenerative disorder characterized by memory and cognitive decline.(Kochman et al. 2025) It is the most common form of dementia, abundantly found in the aging population.(Pardo-Moreno et al. 2022) It is estimated that more than 50 million individuals are suffering from dementia worldwide (Gustavsson et al. 2023). It was discovered by Dr Alois Alzheimer in 1906 (Thakor et al. 2024).

While the exact cause of Alzheimer's disease is yet to be established, two principal pathological hallmarks have been defined: aggregation of extracellular amyloid-β (Aβ) protein and the presence of hyperphosphorylated tau protein in neurofibrillary tangles (NFT), leading to degeneration of an AD patient's brain (Martins et al. 2023). There are various hypotheses proposed for AD, including the amyloid-β hypothesis, neuroinflammatory hypothesis, tau hypothesis (Garbuz et al. 2021)and the cholinergic hypothesis (Chen et al. 2022). The amyloid-β hypothesis suggests that disruption in clearance of amyloid precursor protein leads to accumulation of amyloid-β peptides into extracellular plaques (Ma et al. 2022). While the neuroinflammatory hypothesis states that disease progression is caused by continuous activation of microglia, which, although initially helps in the removal of amyloid-β, subsequently releases pro-inflammatory mediators accelerating neuron damage (AmeliMojarad and AmeliMojarad 2024). In the tau hypothesis, hyperphosphorylation of the microtubule-associated tau protein results in its dissociation from microtubules and

aggregation in the form of neurofibrillary tangles (Rawat et al. 2022). Among these, the cholinergic hypothesis was the first to outline the pathogenic mechanisms of AD (Zhang et al. 2024). The cholinergic hypothesis was based on the observation that there was a notable decline in acetylcholine (ACh) and cholinergic neuron levels in AD patients' brains (Nasb et al. 2024). The cholinergic system is involved in cognitive processes including learning, memory, and attention. Its degradation leads to cognitive decline (H Ferreira-Vieira et al. 2016; Yan et al. 2022). The cholinergic hypothesis was the basis for the first pharmacological strategy, producing acetylcholinesterase (AChE) inhibitors as the first-generation Alzheimer's medications (Behl 2023). Among the sources researched for new AChE inhibitors, natural products have attracted significant attention, as plant-derived alkaloids and phytoconstituents have repeatedly shown potent AChE inhibitory activity alongside comparatively favourable safety profiles relative to synthetic candidates (Gajendra et al. 2024) .

Galantamine is a reversible acetylcholinesterase (AChE) inhibitor which exhibits its therapeutic response by increasing acetylcholine levels in the brain, resulting in improved cognitive ability and better memory (Kalola et al. 2026; Silva et al. 2023). It is a tertiary alkaloid of natural origin, isolated from bulbs of the *Caucasian snowdrop*, *Galanthus woronowii*, and now obtained industrially from several other Amaryllidaceae species, including *Leucojum aestivum* and cultivated Narcissus varieties, alongside chemical synthesis (Koirala et al. 2022). Though well-known for cholinergic relevance, natural AChE inhibitors have several bioactive components in Laggera pterodonta that remain mostly undiscovered at the molecular level, with little or no computational data to justify their inhibitory potential or forecast their pharmacokinetic behaviour.

In the present study, five naturally occurring sesquiterpenoids from a single plant source, Laggera pterodonta: Laggeranine A, Laggeranine B, Pterodontic Acid, Pterodontriol A, and Ilicic Acid (Getahun et al. 2019; Li et al. 2023), are referred to as HM-1 to HM-5, respectively, as shown in Figure 1. These compounds were selected because, although they have been isolated and screened against AChE experimentally to the best of our knowledge no computational study of them has been reported. They were selected for detailed *in silico* investigation, using galantamine, a well-known anti-Alzheimer's drug, as the reference standard. Along with global reactivity metrics such as chemical hardness and softness, Density functional theory (DFT) computations were performed to determine the electronic structure and reactivity of these compounds by frontier molecular orbital (FMO) analysis, molecular electrostatic potential (MEP) mapping, reduced density gradient–non-covalent interaction (RDG-NCI) analysis, Electron localization function (ELF), and projected density of states

(PDOS). Although ADMET predictions were carried out to assess their pharmacokinetic and toxicological suitability as possible candidate drugs, molecular docking was then employed to ascertain the binding affinity and interaction pattern of each molecule with the AChE active site. To go beyond the rigid-receptor approximation of docking, a 300 ns molecular dynamics simulation with MM-GBSA free-energy calculations was performed for the AChE–Laggeranine A (HM-1) complex to assess its dynamic stability and binding energetics. This combined computational strategy seeks to offer mechanistic insight into the AChE inhibitors.

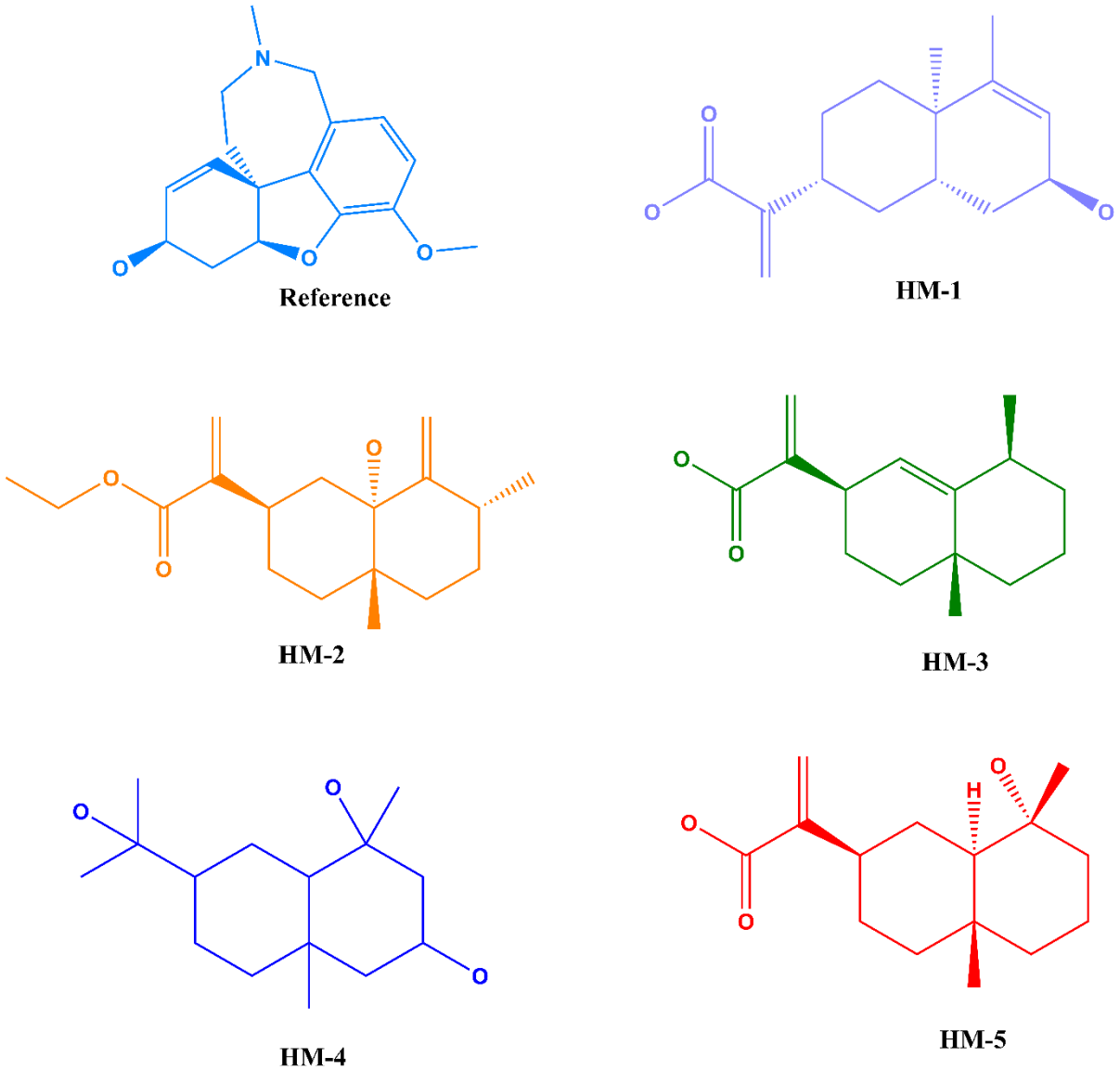


Fig 1 Scheme of **HM-1** to **HM-5** and galantamine.

2. Computational Methodology

2.1.Selection of DFT Level

The reference Galantamine was first optimized using four distinct levels: B3LYP, CAM-B3LYP, ωB97XD, and MPW1PW91, with the basis set 6-311G (d, p). UV/Visible analysis was

carried out at the same functionals noted above in methanol solvent following reference compound optimization. The absorption maximum values for the reference in methanol solvent were 272.33, 249.73, 263.61, and 250.47 nm, at the above-mentioned functionalities coupled with the 6- 311 G (d, p) level (Figure 2). The experimental value of λ_{max} for reference was 288nm.(Taşpınar and Bulduk 2022) The B3LYP level, along with 6- 311 G (d, p), was selected for further evaluation as it gives the result closest to the experimental λ_{max} value.

2.2.DFT Calculations

Molecular properties were extensively investigated utilizing advanced computational techniques. Molecular behaviour was examined through quantum chemical calculations in Gaussian 09W(Gaussian 09 2016)To visualise the results obtained from the input, GaussView 6.0 was used as a key tool. To evaluate the electronic properties of molecules for a broad analysis, the Density Functional Theory (DFT) computational simulation approach was employed for all molecules at the B3LYP functional level, combined with the 6-311G (d, p) basis set. The main aim was to investigate the electronic properties of the reference molecule, designated as (GTM), as well as a series of Natural molecules(Rashid et al. 2023).

The absorption maximum of each molecule was calculated based on the calculation of the molecule when dissolved in a solvent phase, utilizing a conductor-polarizable continuum model (CPCM) to perform the computational calculations in a methanol solvent(Abdelaziz et al. 2023). Reference as well as Natural compounds were investigated using Molecular electrostatic potential plots (MEP), Global reactivity descriptors, reduced density gradient, non-covalent interaction plots (RDG/NCI), and Electron localization function plots. The ELF and NCI were analyzed by Multiwfn(Lu 2024), while VMD (Humphrey et al. 1996)was used for NCI visualization.

2.3. Molecular Docking

For the molecular docking analysis, the crystallographic structure of human acetylcholinesterase (AChE) complexed with Galantamine (PDB ID: 4EY6)(Cheung et al. 2012) was obtained from the Protein Data Bank (PDB) (https://www.rcsb.org/). The co-crystallized ligand, chain B, solvent, and unnecessary molecules were removed by PyMOL (Schrodinger 2015) for docking studies. The chemical structures of the five investigated eudesmane-type sesquiterpenoids naturally occurring in *Laggera pterodonta*—specifically Laggeranine A, Laggeranine B, Ilicic Acid, Pterodontic Acid, and Pterodontriol A—along with the reference alkaloid compound, Galantamine, were compiled for this study.

The target molecular structures were manually sketched in ChemDraw based on the validated configurations reported in the literature. These 2D drawings were subsequently imported into Chem3D (conversion into three-dimensional formats, followed by geometric optimization and energy minimization to ensure accurate spatial conformation before molecular docking simulations. The optimized ligand structure was saved and imported into PyRx, where they were automatically converted into PDBQT format. The AutoDock Vina (Trott and Olson 2010) engine integrated into PyRx was used to perform the Molecular docking simulation. The spatial position of the co-crystallized ligand inside the active site helped to define the grid box's dimensions and center, hence guaranteeing an exact depiction of the binding pocket. To improve the reliability and convergence of the projected binding poses, molecular docking was run with an exhaustiveness level of 64. Using Discovery Studio Visualizer 2025, the produced docked complexes together with their related intermolecular interactions were then investigated and visualized (BIOVIA 2025).

2.4.Molecular Dynamics Simulations

The top-ranked docked pose of HM-1 in complex with acetylcholinesterase (AChE; PDB ID: 4EY6, chain A) was selected as the starting structure for molecular dynamics (MD) simulations. The ligand was prepared using the CHARMM-GUI Ligand Reader & Modeler (Lee et al. 2015)with the CHARMM General Force Field (CGenFF, version 5.0)(Brooks et al. 2009) for atom typing and assignment of partial charges. The protein was assigned the CHARMM36 additive force field within GROMACS(Abraham 2025; Abraham et al. 2015; Bekker et al. 1993). The protein-ligand complex was centred in a rhombic dodecahedral simulation box, maintaining a minimum distance of 1.0 nm between the solute and the box boundaries. The system was solvated using TIP3P water molecules, followed by the addition of Na^+ and Cl^- ions via the GROMACS genion utility to neutralize the net charge and achieve a physiological ionic concentration of 150 mM NaCl. Energy minimization was performed using the steepest-descent algorithm. This was followed by 100 ps of NVT equilibration at 300 K using V-rescaling, then 100 ps of NPT equilibration at 300 K and 1 bar using Berendsen coupling. A 300 ns restraint-free production MD simulation was then performed with a 2 fs timestep. Bonds involving hydrogen atoms were fixed using LINCS, electrostatics were treated using PME with a 1.2 nm cutoff, and van der Waals interactions were switched off between 1.0–1.2 nm. Periodic boundary conditions were employed, and coordinates were saved every 10 ps for analysis. Graphs were plotted using XMGRACE.

2.5. Binding Free Energy Calculations (MM-GBSA)

Binding free energy calculations were assessed using the Molecular Mechanics/Generalized Born Surface Area (MM-GBSA) method as executed in gmx_MMPBSA (v1.6.5)(Valdés-Tresanco et al. 2021). Fifty snapshots were collected at 3-ns intervals from the 150–300 ns interval of the production period to confirm that calculations were based on the structurally equilibrated system. The analysis employed a single-trajectory approach, with polar solvation energies calculated through the Generalized Born model (igb = 5, salt concentration = 150 mM) and non-polar contributions estimated from the solvent-accessible surface area. The entropic contribution to binding was evaluated using the Interaction Entropy (IE) approach, while per-residue energy decomposition was analysed for residues located within 4 Å of the ligand.

2.6.ADMET

Finally, the pharmacokinetic (ADME) and toxicity profiles of the investigated compounds were evaluated using ADMETlab 3.0 (Fu et al. 2024) and ProTox 3.0 (Banerjee et al. 2024), respectively.

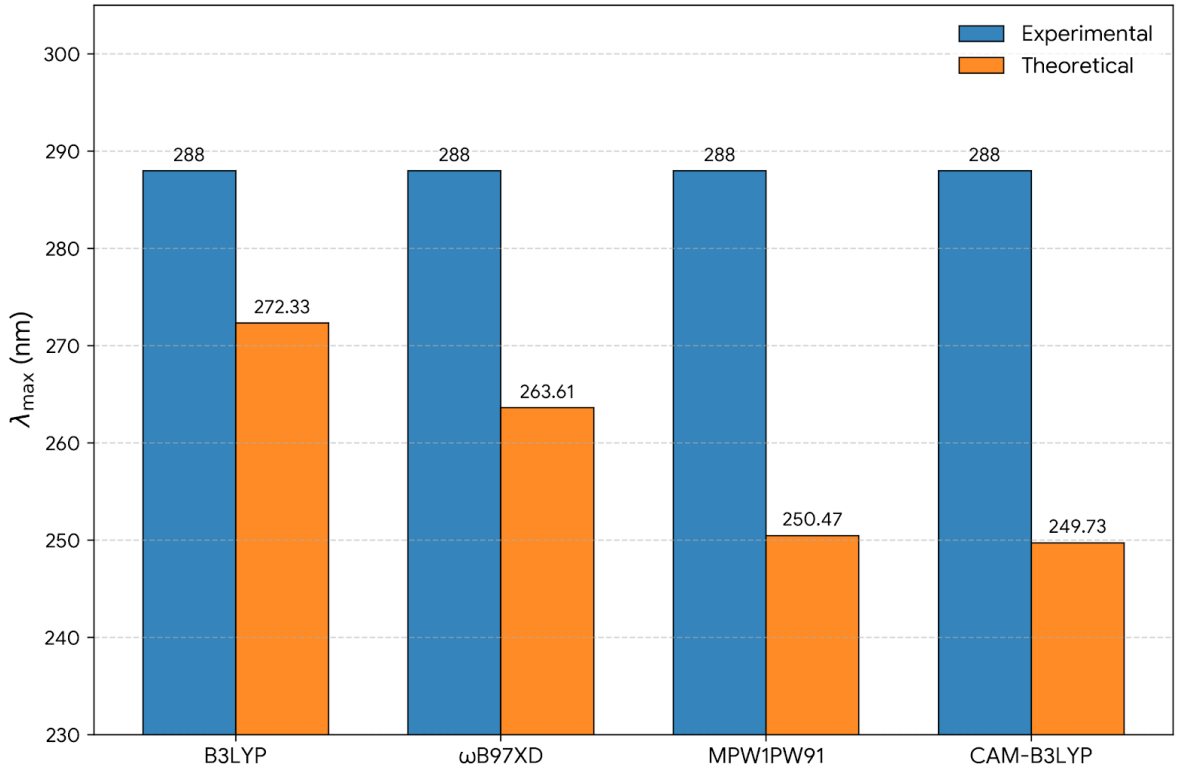


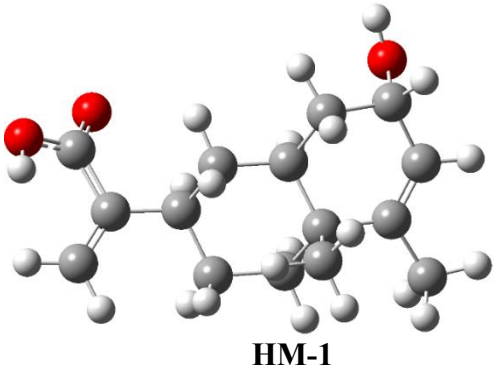
Fig 2 Benchmark of DFT functionals against experimental UV-Vis absorption maximum (λ_{max}).

3. Results and Discussions

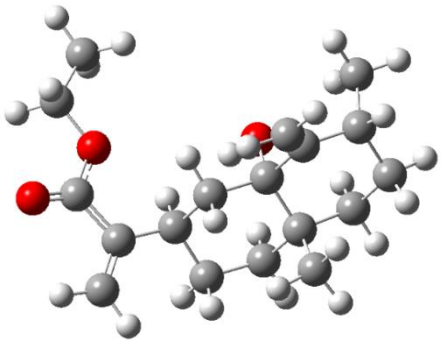
3.1.Frontier Molecular Orbital (FMO) Analysis

Evaluation of Frontier Molecular Orbitals (FMO) provides important information about molecule stability and reactivity. The highest occupied molecular orbital (HOMO) and lowest unoccupied molecular orbital (LUMO) reflect the electron-donating and electron-accepting capacity of molecules. The difference in energy between HOMO and LUMO defines the energy gap (ΔE). One of the main factors used to forecast reactivity and stability is this one (Hussein and Fadhil 2023). A lower ΔE shows increased reactivity and lesser stability of molecules, while a wider gap shows less reactivity and more stability (Bakheit et al. 2024).

FMO calculations were performed for all references along with the investigated Natural products **HM-1, HM-2, HM-3, HM-4, and HM-5** by utilizing the B3LYP level along with the 6-311G (d, p) basis set. DFT-optimized structures of R and HM-1 to HM-5 are shown in Figure 3. The LUMO distribution of natural compounds showed minimal alteration compared to R. In **HM-1, HM-2, HM-3, and HM-5**, the acceptor density moved toward the ester carbonyl/oxygen-bearing moiety of the saturated ring framework, while in R, the LUMO was still concentrated over the aromatic ring and the nearby methoxy-substituted region. The LUMO in **HM-4** moved more towards the hydroxyl/epoxide-bearing region because of this oxygenated site's increased electron-withdrawing nature. The HOMO of R was largely restricted to the saturated ring core, suggesting that in the absence of extended conjugation, this non-aromatic framework serves as the main electron donor site, whereas in the natural compounds, it was primarily localized on the aromatic ring and its adjacent oxygenated substituent. In **HM-4,** the HOMO was localized on one face of the decalin ring, owing to the reduced donor contribution of the oxygenated moiety. The fading orders for LUMO and HOMO were **R<HM-1<HM-2<HM-3<HM-5<HM-4** and **R<HM-1<HM-2<HM-3<HM-5<HM-4**, respectively. The energy band gap (ΔEg) for R and the DDs (HM-1 to HM-5) was 4.209, 4.412, 5.202, 5.244, 5.605, and 7.347 eV, respectively (Table 1). The distributions of electron density in the HOMO and LUMO of the reference and all natural compounds are shown in Figure 4.



HM-1



HM-2

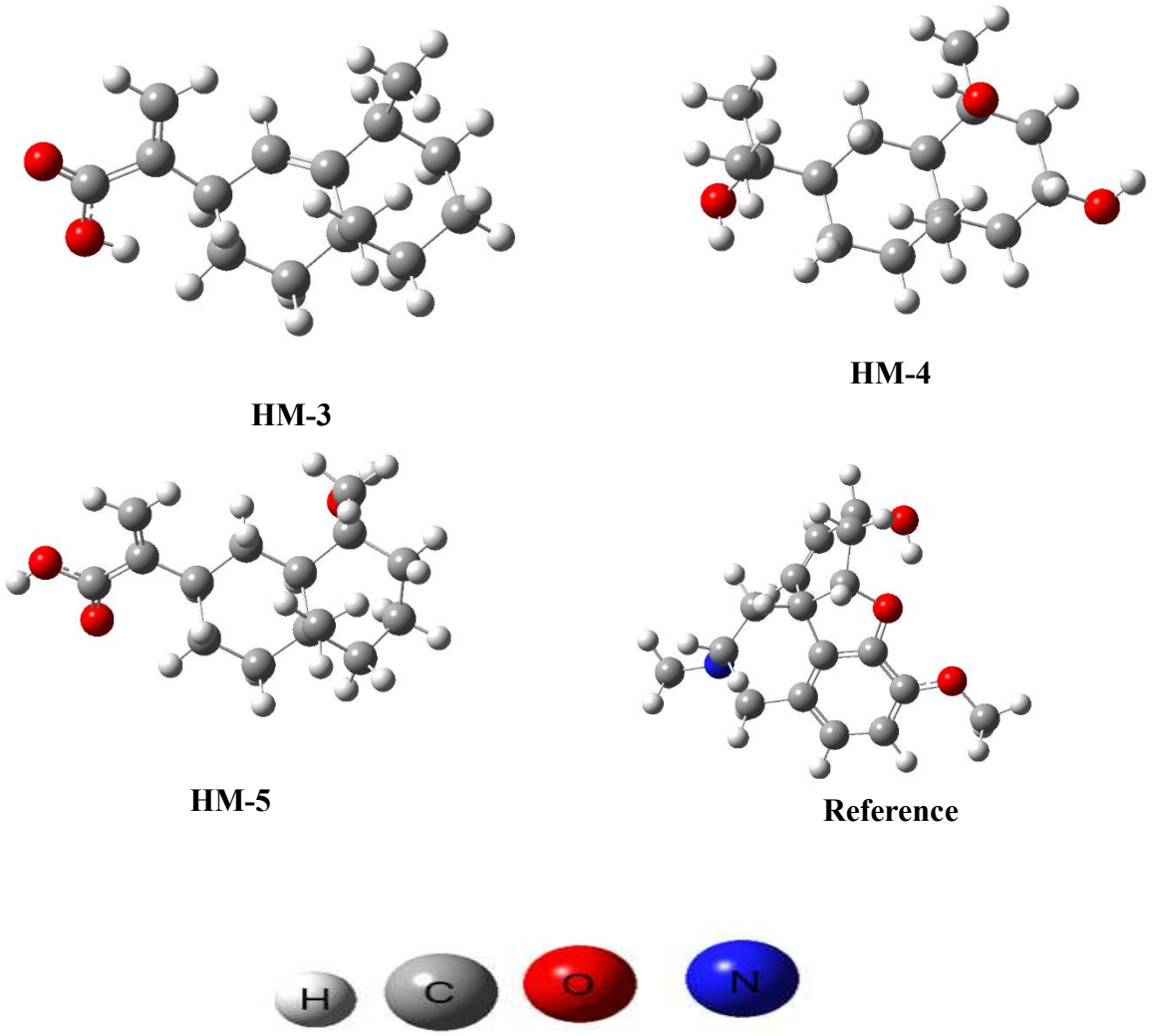


Fig 3 Representation of optimized 3D structure of the reference (**R**) and natural compounds **HM-1 – HM-5**.

Table 1. Frontier molecular orbital energy levels (E_{HOMO}, E_{LUMO}) and regional energy bandgap parameters computed for the reference drug (**R**) and **HM-1** through **HM-5**.

Compound	**HOMO (eV)**	**LUMO (eV)**	**Gap (eV)**
Reference	-4.508	-0.299	4.209
HM-1	-6.353	-1.941	4.412
HM-2	-6.881	-1.679	5.202
HM-3	-6.894	-1.649	5.244
HM-4	-6.859	+0.488	7.347
HM-5	-7.211	-1.606	5.605

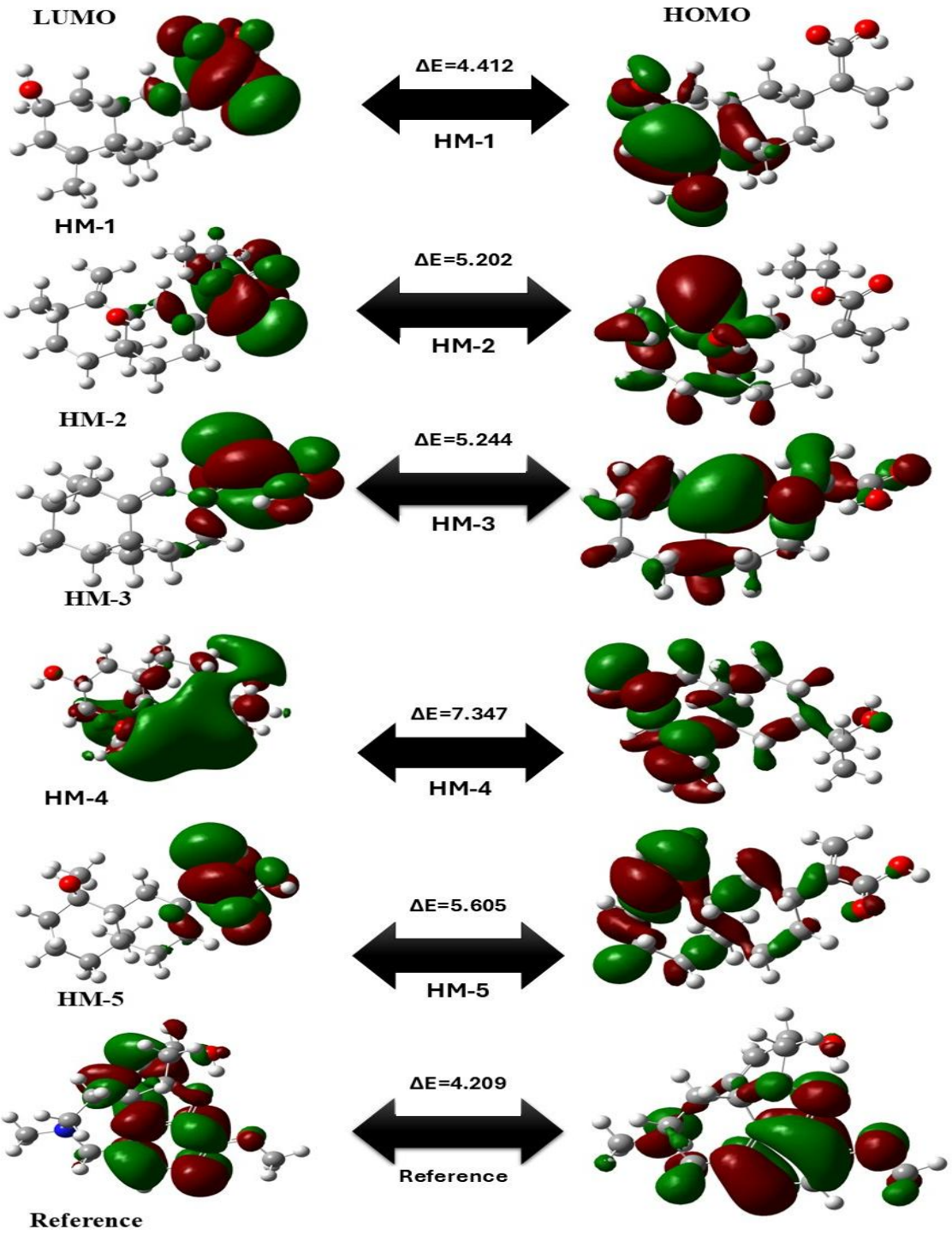


Fig 4 Frontier molecular orbital (HOMO and LUMO) electron density distribution patterns for the reference compound (**R**) and natural compounds **HM-1** to **HM-5**.

3.2.Optical properties

Time-dependent density functional theory (TD-DFT) best captures optical characteristics that show how a molecule interacts with light, especially in the UV-visible range, by predicting excitation energies, absorption wavelengths, and oscillator strengths for transitions between

ground and excited states. Unlike the fixed HOMO–LUMO gap, TD-DFT considers electron-hole interaction during excitation, therefore giving a more accurate representation of the actual absorption behavior of a molecule. Every excited state shows the electronic source of its optical character by its excitation energy (Ex, eV), wavelength (λ_{max}, nm), oscillator strength (f), and the orbitals implicated (Akman and Kutlu 2025). The absorption maxima (λ_{max}) for R and the natural compounds (**HM-1 to HM-5**) were computed using the CPCM solvation model. This made use of B3LYP and the 6-311G (d, p) basis set; methanol was chosen as the solvent for computing. The theoretical λ_{max} value for R was calculated as 272.33 nm, compared to its experimental value of 288 nm, indicating reasonably good agreement between theory and experiment. And **HM-2** was calculated at 197.25 nm and 196.82 nm, respectively, both in close agreement with their reported experimental value of 195 nm. The λ_{max} values for **HM-3, HM-4**, and **HM-5** were calculated as 281.30, 175.48, and 252.13 nm, respectively (Table 2). Relative to **R, HM-3** exhibited a bathochromic (redshift) shift to a longer wavelength, likely due to the conjugation between its ring double bond and the adjacent acrylate ester's C=C–C=O system, which narrows the HOMO–LUMO gap for the dominant transition. While **HM-1, HM-2, HM-4, and HM-5** all showed hypsochromic (blueshift) shifts towards a higher-energy region, **HM-4** showed the most notable blueshift throughout the series. The increasing order of absorption maxima (λ_{max}) for R and the natural compounds was **HM-4 < HM-2 < HM-1 < HM-5 < R < HM-3. Table 2** lists the excitation energies and oscillator strengths (f) for R and **HM-1** to **HM-5**. With lower and more varied oscillator strengths, between 0.0002 (**HM-5**) to 0.0331 (**HM-2**), The natural products showed limited to moderate transition intensities (f = 0.0383 for R), ranging from 0.0002 (**HM-5**) to 0.0331 (HM-2, closest to R). While R, **HM-3**, and **HM-4** were dominated by HOMO→LUMO transitions (91%, 98%, 80%), **HM-1**, **HM-2**, and **HM-5** arose mainly from deeper occupied orbitals (H-5→LUMO, H-1→L+1, H-3→LUMO), indicating minimal frontier HOMO contribution. Dipole moments ranged from 2.07 D (HM-2) to 6.44 D (HM-3), reflecting differing polarity across the series.

. **Table 2.** Calculated in the solvated state predicted photodynamic properties and optical characteristics of the reference drug (**R**) and natural compounds (**HM-1–HM-5**).

Compound	**λ_{max} (nm)**	**Experimental Value (nm)**	**E_x (eV)**	***f***	**Major Assignment**	**Dipole solvent (Debye)**

Reference	272.33	288	4.553	0.0383	HOMO->LUMO (91%)	5.04
HM-1	197.25	195	6.286	0.0015	H-5->LUMO (92%)	6.36
HM-2	196.82	195	6.300	0.0331	H-1->L+1 (74%)	2.07
HM-3	281.30		4.408	0.0107	HOMO->LUMO (98%)	6.44
HM-4	175.48		7.066	0.0159	HOMO->LUMO (80%)	2.41
HM-5	252.13		4.917	0.0002	H-3->LUMO (41%)	3.42

3.3. Global Hardness and Global Softness

The two important indicators of reactivity based on the concept of density functional theory (DFT), global hardness (η) and global softness (S), suggest the resistance of a molecule to fluctuations in electron density. Greater hardness indicates greater stability and lesser reactivity. Softer molecules generally exhibit greater reactivity and charge transfer capability. So, softness is the inverse of hardness and signifies the ease with which the electron density of a molecule can be polarized. These factors are calculated from the energy levels of frontier orbitals as follows: $\eta = (E_LUMO - E_HOMO)/2$ and $S = 1/(2\eta)$ (Allal et al. 2024; Chaudhary et al. 2021). The computed band gap, global hardness, and global softness for Reference and all the natural Compounds (**HM-1 to HM-5**) are presented in Table 3. The reference compound showed the lowest value for band gap (4.209 eV), thus the lowest hardness (2.105 eV) and highest softness (0.2376 eV^{-1}), which means that the compound had the most polarizable electronic arrangement and the highest reactivity within the series of the six compounds. **HM-1** shows resemblance to the reference; it had a slightly higher band gap value (4.412 eV), yet similarly low hardness and high softness values, suggesting almost similar reactivity to the reference. However, **HM-2, HM-3,** and **HM-5** had progressively larger band gaps (5.202, 5.244, and 5.605 eV, respectively), thus higher hardness and lower softness values, which is an

indication of a comparatively stable compound with low polarity within the electronic arrangement. The largest band gap value of all compounds was observed in **HM-4** (7.347 eV); for that reason, **HM-4** had the highest hardness (3.674 eV) and the lowest softness (0.1361 eV^{-1}). Overall, the hardness/softness trend followed the order **R < HM-1 < HM-2 < HM-3 < HM-5 < HM-4**, closely paralleling the band gap trend, and confirming that compounds with a narrower HOMO–LUMO gap (reference and **HM-1** possess a softer, more reactive electronic character, while **HM-4**, with its markedly wider gap, stands out as the most kinetically stable and least reactive candidate in the series. Across the series, HM-1 most closely matched reference reactivity (ΔE = 4.412 vs. 4.209 eV; S = 0.2266 vs. 0.2376 eV^{-1}), predicting the suitable enzyme inhibition. HM-2, HM-3, and HM-5 showed gradually lower softness and moderate reactivity, while HM-4's highest hardness (3.674 eV) and lowest softness (0.1361 eV^{-1}) making it as the least reactive and weakest predicted inhibitor.

Table 3. Calculated global conceptual DFT descriptors, chemical hardness (η) and softness (S), for the reference compound (**R)** and natural compounds **HM-1** to **HM-5**.

Compound	**Band Gap (ΔE, eV)**	**Hardness (η, eV)**	**Softness (S, eV^{-1})**
Reference	4.209	2.105	0.2376
HM-1	4.412	2.206	0.2266
HM-2	5.202	2.601	0.1922
HM-3	5.244	2.622	0.1907
HM-4	7.347	3.674	0.1361
HM-5	5.605	2.803	0.1784

3.4.Global Reactivity Descriptors

Derived from conceptual density functional theory (DFT), global chemical reactivity descriptors offer quantitative metrics of a molecule's general stability, tendency for electron-donating and electron-accepting, and susceptibility to chemical interactions (Muya et al. 2019). Koopmans' theorem-derived parameters (IP, EA, μ, χ, ω, ΔNmax) characterize a molecule's electron-donating/accepting tendencies: μ and χ indicate the direction of electron flow, while higher ω reflects greater capacity to accept electron density from a nucleophile. Together, these descriptors clarify the relative reactivity, stability, and binding potential of the studied compounds (Tiéba et al. 2023). The calculated global reactivity descriptors ionization potential (IP), electron affinity (EA), chemical potential (μ), electronegativity (χ), electrophilicity index

(ω), and maximum charge transfer capability (ΔN_{max}) for the reference and the investigated natural compounds (**HM-1–HM-5**) are presented in Table 4. The reactivity indicators suggest that the reference compound showed the lowest values of IP (4.508 eV) and EA (0.299 eV) together with low electronegativity (2.404 eV) and electrophilicity index (1.372 eV). This suggests that this compound shows the least tendency to accept electrons and is thus the richest and most nucleophilic of the six compounds. **HM-1** had the highest value of electrophilicity index (3.899 eV) and maximum ΔN (1.880). This confirms that it is the most electrophilic species with maximum charge-accepting potential. The **HM-2** and **HM-3** structures are very similar, having high values of the electronegativity (4.280 and 4.272 eV, respectively) and electrophilicity index (3.522 and 3.480 eV, respectively), indicating that these have high electron acceptor properties. The **HM-4** structure was completely different, since it had a negative EA value (−0.488 eV) due to the positive energy of the LUMO, together with the lowest electrophilicity index (1.381 eV) and the low ΔNmax value (0.867), which justifies the largest HOMO-LUMO gap between the natural extracts. As a result, this structure is the most electronically stable and electrophilic compound. The **HM-5** molecule had the highest value of the ionization potential (7.211 eV) and moderately electronegativity (4.409 eV) but still had an electrophilicity index of (3.468 eV). Overall, **HM-1, HM-2, HM-3,** and **HM-5** emerged as comparably strong electrophiles with electrophilicity indices exceeding that of the reference compound, while HM-4's markedly lower electrophilicity and higher stability distinguish it as the electronic outlier within the series. Reference shows a distinct electron-donating profile (low IP = 4.508 eV, ω = 1.372 eV) versus the sesquiterpenoids. HM-1 has the highest electrophilicity (ω = 3.899 eV) and ΔNmax (1.880), predicting the suitable inhibitory potential, followed by HM-2, HM-3, and HM-5 with comparably high but lower electrophilicity (ω ≈ 3.47–3.52 eV); HM-4's negative EA (−0.488 eV) and lowest ω (1.381 eV) mark it as the weakest electron acceptor.

Table 4. Computed conceptual DFT descriptors, including ionization potential (IP), electron affinity (EA), chemical potential (μ), electronegativity (χ), electrophilicity index (ω), and maximum charge transfer ($\Delta N_{\max}$), for reference (**R**) and natural compounds **HM-1** to **HM-5**

Compound	**IP (eV)**	**EA (eV)**	**μ (eV)**	**χ (eV)**	**ω (eV)**	**ΔN_{max}**
Reference (Galantamine)	4.508	0.299	-2.404	2.404	1.372	1.142
HM-1	6.353	1.941	-4.147	4.147	3.899	1.880

HM-2	6.881	1.679	-4.280	4.280	3.522	1.646
HM-3	6.894	1.649	-4.272	4.272	3.480	1.629
HM-4	6.859	-0.488	-3.186	3.186	1.381	0.867
HM-5	7.211	1.606	-4.409	4.409	3.468	1.573

3.5. Molecular Electrostatic Potential

MEP analysis shows important electrophilic and nucleophilic sites where chemical reactions are most likely to take place by detailing molecular directionality and charge distribution (Rajesh et al. 2025). It is useful for identifying reactive sites towards electrophilic/nucleophilic assault and hydrogen bonding, red/yellow indicates electron-rich (negative) regions, blue/light blue indicate electron-poor (positive) areas, and green marks neutral (zero-potential) regions on the MEP surface visualizes molecular charge distribution and polarity. (Sumathi et al. 2025). The MEP graphs of Reference and the investigated natural products (**HM-1–HM-5**) are exhibited in Figure 5. In Reference, the negative potential was concentrated around the hydroxyl and methoxy oxygens, while a weaker positive potential surrounded the tertiary amine nitrogen. In **HM-1,** the negative potential was localized over the acrylate carbonyl oxygens, while the positive potential was delocalized across the left side and top-right region of the decalin core. In **HM-2,** the negative potential was centred on the ester carbonyl and adjacent hydroxyl oxygens, with no significant positive region elsewhere, reflecting an overall electron-poor skeleton. In **HM-3,** the negative potential was sharply localized around the ethyl ester carbonyl on the right side, with a weaker contribution from the epoxide oxygen, while the rest of the framework remained largely neutral. The negative potential was localized in the upper left part of **HM-4** on the hydroxyl/epoxide oxygens, while the positive part was on the opposite right side. For **HM-5,** the negative potential is clustered in the centres on the epoxide and ester carbonyl oxygens, while the positive potential is assembled in the upper left corner and far-right corner of the molecule. Generally, the negative potential was always on the oxygen atoms (ester carbonyls, hydroxyls, epoxides), which are determined as the main nucleophilic centres, while the positive is diffusely spread across the alkyl/methyl parts of the decalin-like framework. The same pattern is observed in Reference. The negative potential localizes oxygen atoms (carbonyls, hydroxyls, epoxides) across all compounds, marking key nucleophilic sites, mirroring reference patterns. HM-1 and HM-5 show charge distributions favoring active-site binding, HM-2 and HM-3 display comparable electrostatic profiles, while HM-4's more separated charge regions suggest weaker electrostatic suitability.

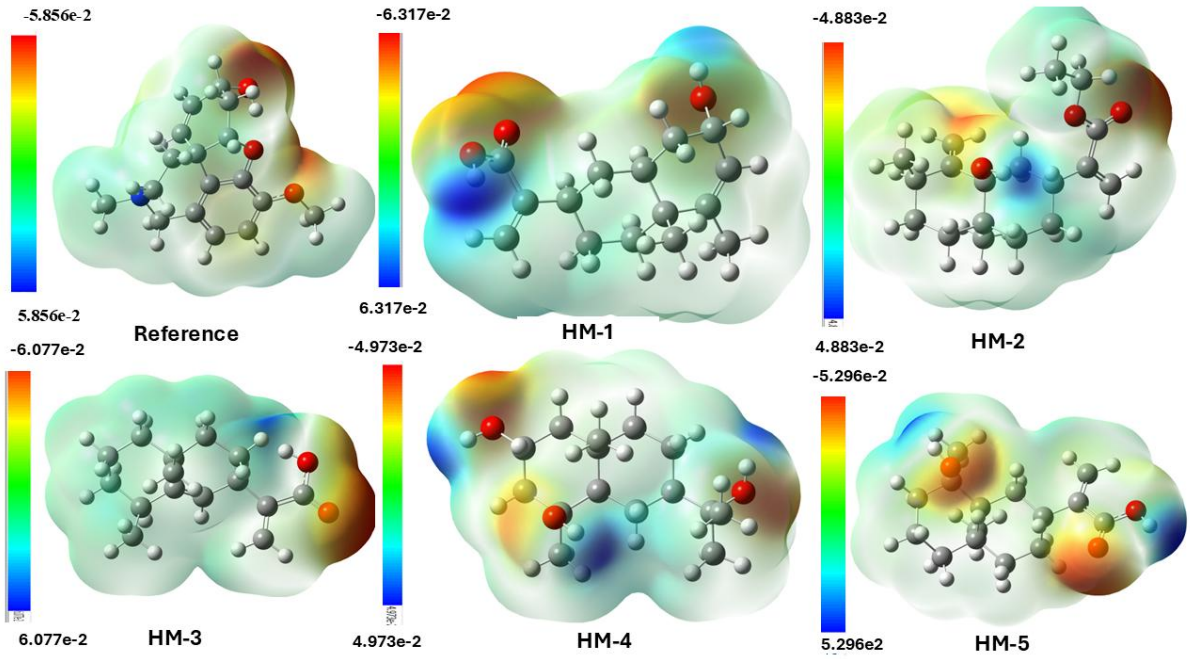


Fig 5 MEP surface maps for the reference compound (R) and natural extracts (HM-1, HM-2, HM-3, HM-4, HM-5) were generated based on DFT calculations.

3.6.Total Density of States (TDOS)

Multiwfn software was used to obtain the combined TDOS/PDOS/OPDOS plot, where the black TDOS line indicates the overall energy level distribution and HOMO/LUMO positions, while the PDOS curves show the percentage contributions of donor and acceptor fragments. which are represented by different colored lines. The blue line represents the acceptor and the red line the donor fragment, while the green OPDOS line indicates bonding, non-bonding, or anti-bonding character between them. Positive values show positive cohesion, negative values show negative convergence, and values near zero show non-bonding interactions. Between HOMO/LUMO, each framework has a unique energy gap; larger gaps are linked to lower ICT and perhaps lower reactivity. The results are shown below in (figure 6). The results showed that the **HM-4** molecule exhibited a positive OPDOS due to its function as an electron donor. The electron density on the aromatic ring was increased by the presence of electron-donating groups like OH and CH3 (which exhibit the +M effect). Interestingly, the PDOS results for the **HM-1** molecule were positive. This results from the carboxyl group's dual nature. In the system's conjugation, the carbonyl portion functions as an acceptor and the OH substituent as a donor. Increased ICT will result from positive overlapping. HM-4's largest band gap suggests lower global reactivity, yet its positive OPDOS reflects efficient local charge transfer between OH/CH3 groups and the ring, favouring localized enzyme interactions. HM-1's dual donor-

acceptor character (OH donor, carbonyl acceptor) similarly enhances ICT, supporting its predicted strong binding.

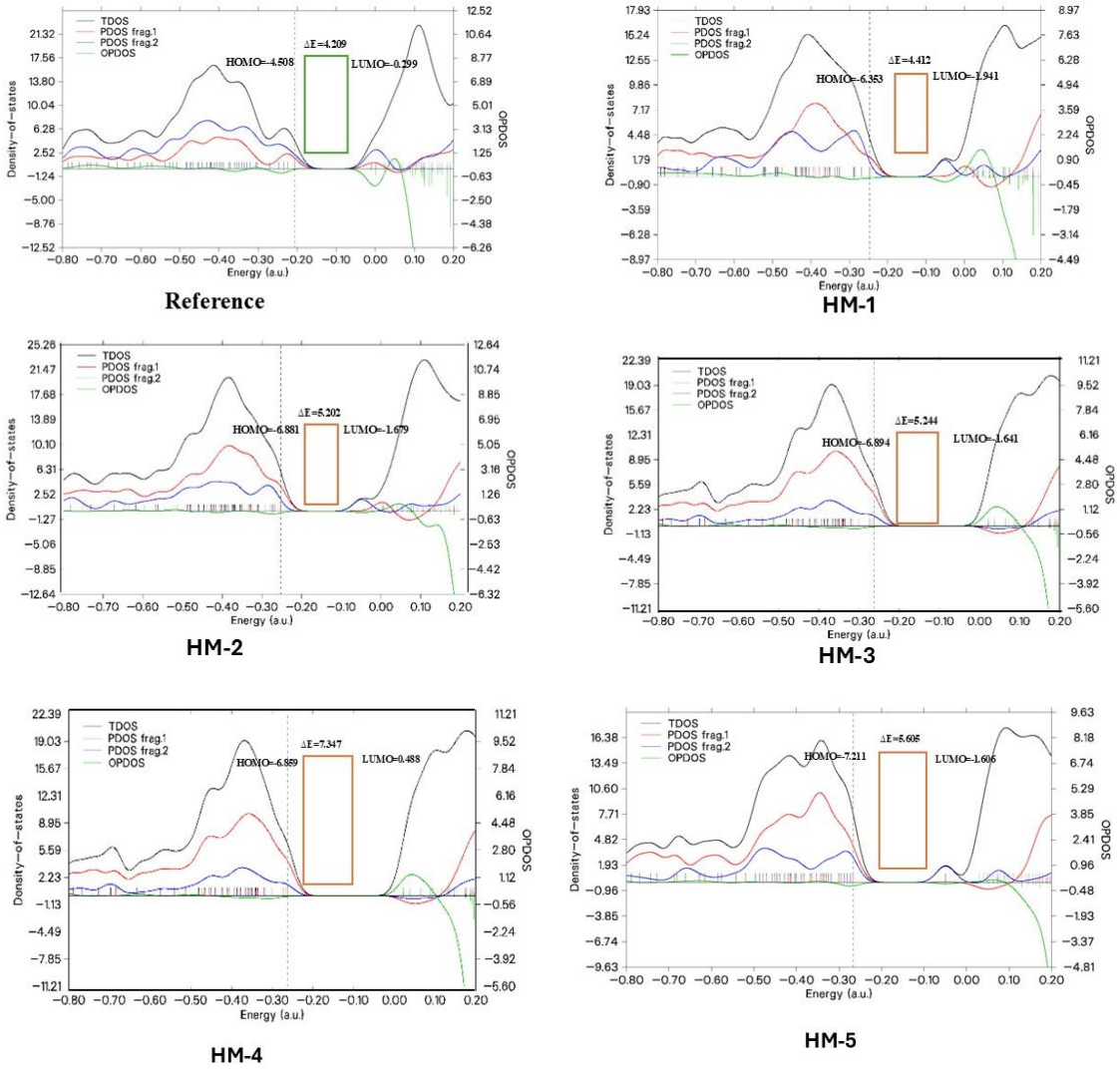


Fig 6 TDOS and OPDOS graphs of HM-1 to HM-5 and R.

3.7. RDG and NCI Analysis of Non-Covalent Interactions

Another effective technique to look at the strength of the bonds and the degree of charge transfer between atoms, reduced density gradient (RDG) and non-covalent interaction (NCI) analysis, was employed. This study shows regions around molecules where homogeneous electrons are more concentrated, and it is derived from basic DFT properties.(Boudjahem et al. 2025) RDG maps and NCI structures are very useful in determining the regions that exhibit attractive and repulsive forces between the atoms in the structure of a compound. This analysis also gives us information about weak van der Waals forces or interactions between the atoms.(Barukial et al. 2026) RDG vs. sign(λ_2)ρ plots (Figure 7) reveal interaction type via the sign of λ_2 and strength via isosurface color: blue denotes attraction, green denotes van der

Waals/hydrogen bonding, and red denotes repulsion. The reference compound showed a typical tripartite pattern, a red spike (repulsion), a green region near zero (van der Waals), and a blue region (attraction) consistent with a balanced noncovalent interaction profile. The same type of pattern, with comparable red spikes, is exhibited in all the (**HM-1 to HM-5**) natural products, indicating that steric repulsion is a key feature of these compounds. The reference molecule showed a great number of green discs across the combined rings and the red-orange patches at the ring fusion around the methoxy-substituted ring, which represent the steric hindrance in addition to dispersion interactions. The **HM-1** molecule also showed considerable green isosurfaces on the fused ring with significant red discs at the positions of ring fusion. The **HM-2** molecule also displayed green spikes over the ring core with a significant red-orange disc at the ester carbonyl oxygens. The **HM-3** molecule had a compressed green isosurface with a red patch at the location of the epoxide oxygen due to strain on the oxirane ring. The **HM-4** extract showed green discs over its alkyl substituent and decalin core, with a red-orange disc around the hydroxyl group. The **HM-5** molecule exhibited a similar pattern, just like **HM-2,** with green spikes over the ring core and a significant red-orange disc around the ester oxygens. At the end, the consistent presentation of the spike network and isosurface configurations in both the reference and the **HM-1** through **HM-5** implies that the natural product also maintain their conformations via an interaction mode comparable to that in reference and notably involving in van der Waals interaction which are helpful in enzymatic interaction and in addition to compounds also exhibit hydrogen bonding/electrostatic interactions and an amount of steric repulsions due to the fused polycyclic systems. Especially, the observation we obtain in this analysis is that the regions of blue, which represent the attractive force, are mainly due to the centres around the ester carbonyl, hydroxyl, and epoxide oxygens in **HM-1** through **HM-5.** These observations are also verified by the investigation of molecular electrostatic potential (MEP) plots. The constant green (van der Waals) and localized red-disc (steric strain) patterns across HM-1–HM-5, mirroring the reference, indicate that compounds can adopt stable, favorable conformations for enzyme binding through similar noncovalent interaction modes. The blue attractive regions centered on ester carbonyl, hydroxyl, and epoxide oxygen further predict these as key sites for hydrogen bonding/electrostatic interactions with enzyme active-site residues.

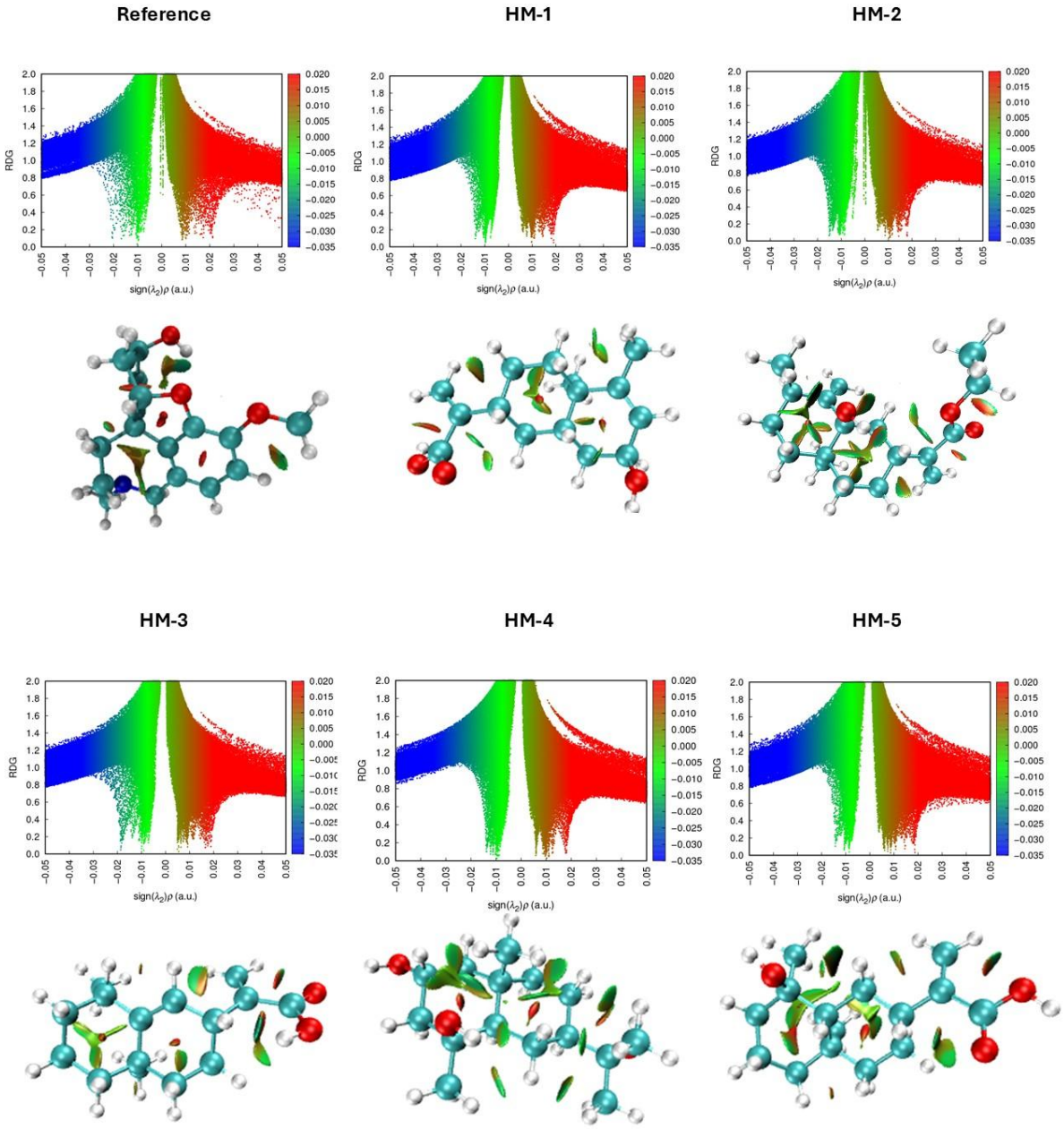


Fig 7 The representation of RDG plots and NCI isosurfaces for Reference and natural compounds **HM-1** through **HM-5.**

3.8.Electron Localization Function

The electron localization function (ELF) is used to visualize the localization and delocalization in the molecule. This analysis offers information about the relationship between the localization of lone pairs, bonding, and core electrons (Dhifet et al. 2025). It also gives information about the areas where there are clustered electrons, such as covalent bonds and lone pairs, along with the regions of delocalized electrons, giving a complete view of the bonding characteristics (Belghalia et al. 2026). It is a dimensionless real space function with values ranging from 0 to 1, (ELF→ 1) means localized electron densities, which can be seen by the red areas in the plot.

(ELF→ 0.5) means delocalized electron densities which are the green areas in the plot, and at the end (ELF→0), the blue areas give information about the low localized electron densities.(Nguyen et al. 2025) The two-dimensional ELF maps of the reference compound and the natural products (**HM-1**–**HM-5**) intended onto the molecular plane are displayed in Figure 8, these maps show distinct regions of electron localization and delocalization distributed across the labelled framework. The reference compound exhibits intense localization focused on the two terminal hydrogen atoms and the oxygen-substituted carbon on the right side of the compound, along with a labelled carbon and oxygen pair close to the ring, while the intermediate ring carbons displayed mostly green, delocalized character. With the surrounding sigma-bonded framework showing good green delocalization dotted with sharp blue borders, **HM-1** showed strong localization at its three labelled ring carbons and at the terminal hydrogen and delocalization at its carbon atoms. Regarding **HM-2**, the labelled oxygen atom, the two adjacent ring carbons, and both terminal hydrogen atoms exhibit lone-pair and C–H bonding character, therefore reflecting high ELF intensity at these areas; the middle ring region remained mainly delocalized. **HM-3** showed a single strong carbon-centered localization site close to the ring core together with a wide, very red hydrogen-associated area at the edge; the rest of the framework showed a green-to-blue delocalization steepness. On the other hand, consistent with its highly substituted, saturated skeleton, **HM-4**, showed several methyl and hydrogen groups, which show the most extensive localization pattern among the series, with red spots at all marked hydrogen atoms and the three labelled ring carbons. With delocalized green areas joining the main ring structure, **HM-5** particularly showed localization at the oxygen atom, three ring carbons, and one terminal hydrogen, also with the delocalization pattern. All the natural compounds along with the reference constantly display strong ELF values at the oxygen and terminal hydrogen regions. All six compounds point to these sites as the main centres of electron localization and lone-pair/covalent bonding character; the inside ring carbons mainly show extensive green-to-blue character, reflecting extended, diffuse bonding density all over the fused ring systems. The strong ELF localization at oxygen/terminal hydrogen sites across all compounds predict directional H-bonding with enzyme residues, while the diffuse green-to-blue delocalization over the ring cores predicts conformational stability favorable for stable binding.

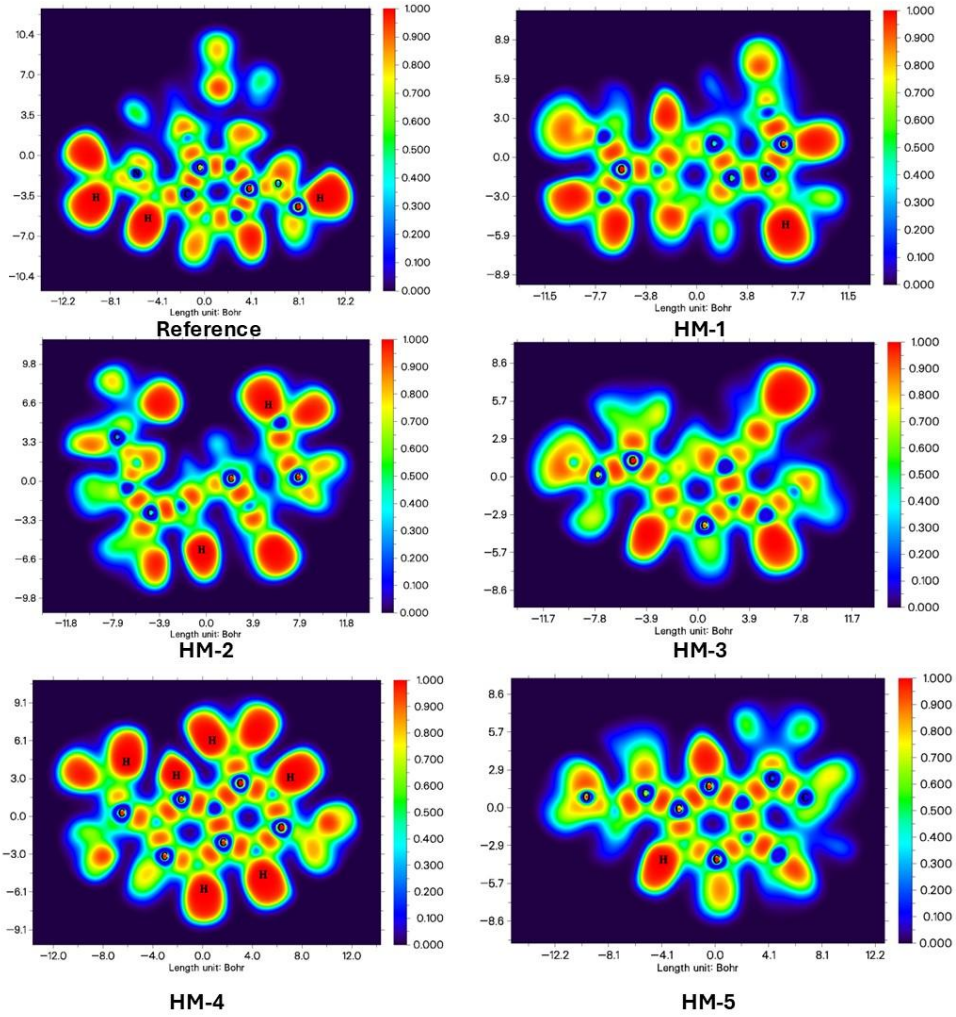


Fig 8 Maps of Electron Localization Function (ELF) of Reference and natural compounds **HM-1** to **HM-5**.

3.9. *In silico* Docking and Binding Energy Analysis

The docking analysis of galantamine (reference) and its derivatives (**HM-1–HM-5**) against the acetylcholinesterase receptor (PDB ID 4EY6) is presented in Table 5. For the docking protocol validation, the co-crystallized ligand was redocked into the active site of the acetylcholinesterase receptor, and the redocked pose shows an RMSD value of 1.97 Å. The binding energy of the reference −10.4 kcal/mol was supported by conventional H-bonds with SER203 (2.86 Å) and GLU202 (2.76 Å), carbon-hydrogen bonds with SER203, HIS447, TYR124, and SER125, and π-sigma/π-alkyl interactions with TRP86, PHE295, PHE297, PHE338, and HIS447, reflecting strong hydrophobic anchoring and consistent with its potent inhibitory activity. The presence of the same interactions that are made by galantamine in the catalytic site gives confidence in the correctness and reliability of the docking method used in this research. On the other hand, **HM-1** showed the highest binding energy among all natural

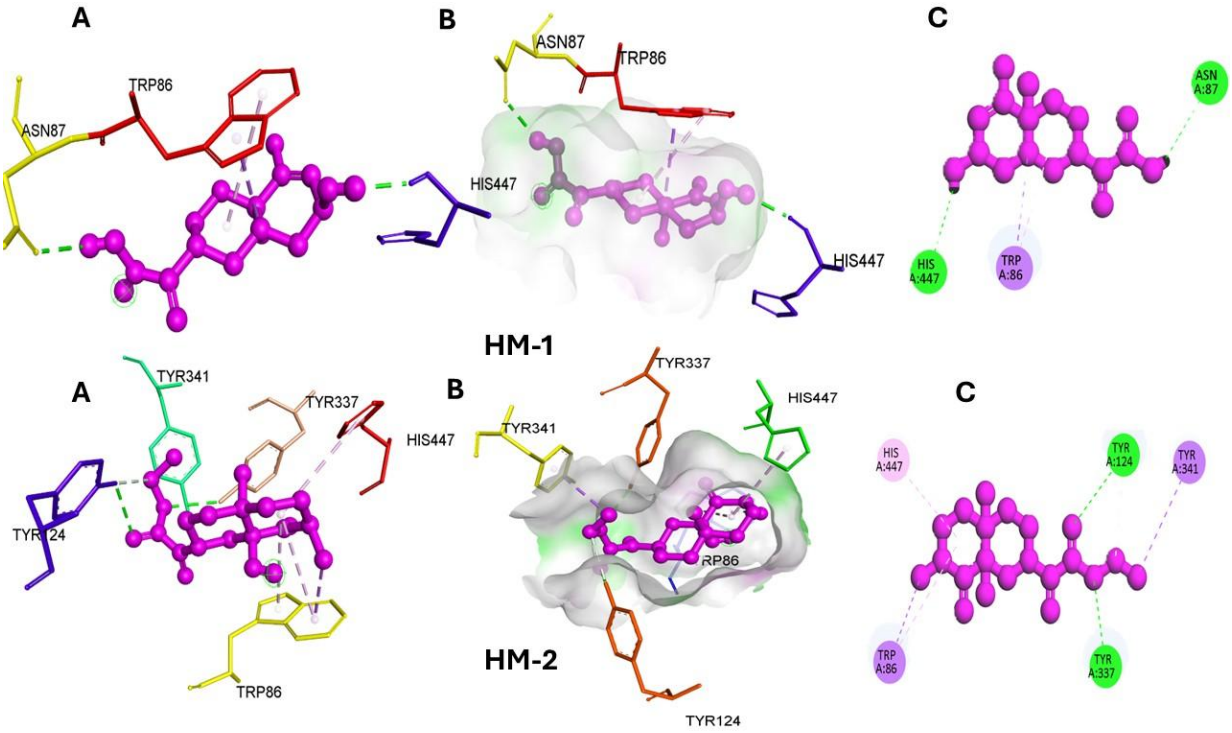
compounds at -8.6 kcal/mol while maintaining foundational interactions that help stabilize the molecule in the receptor pocket. The presence of an ester group and a bicyclic ring system supports in achieving the best position of **HM-1** in the binding pocket. The hydrogen bond interaction with ASN87 was 2.47 Å, and the same interaction but with HIS447 was observed at a distance of 2.13 Å. At 3.87 Å, a π-sigma interaction with TRP86 was also observed. The ester group in the **HM-1** compound helped in the formation of hydrogen bonding with important residues of the enzyme, but due to the absence of other aromatic bonding, in contrast to the reference responsible for its low docking score. **HM-2** showed a docking score of −8.0 kcal/mol and made hydrogen bonding at 3.04 Å with TYR124 and 2.89 Å with TYR337 residues. The carboxylate group present in the **HM-2** determined that the molecular structure might be involved in electrostatic bonding with the positively charged residues lying in the catalytic site. Formation of a carbon-hydrogen bond interaction with the TYR124 residue was at 3.01 Å. Aromatic interactions were through π-sigma interactions with the TRP86 residue at 3.52 Å and the TYR341 residue at 3.93 Å. Hydrophobic interactions were revealed through π alkyl interaction with TRP86. **HM-3** exhibited a binding affinity of −8.3 kcal/mol, featuring conventional hydrogen bonds with TYR337 at 2.85 Å and TYR341 at 3.25 Å. The particularly combined ring structure of **HM-3** that consists of many chiral centres and a ketone group is likely to generate hydrophobic interactions within the aromatic system. A π-π interaction with TRP86 at 3.57 Å and a π-sigma interaction with TYR337 at 3.89 Å were seen. A hydrophobic interaction was given by the π-alkyl interactions with TRP86. The **HM-4** exhibits a binding energy of −8.0 kcal/mol, making conventional hydrogen bonds with TYR337 at 2.96 Å and ASP74 at 2.22 Å. Multiple π-sigma interactions were observed with TRP86 at 3.82 Å, TYR337 at 3.45 Å, and TRP86 again at 3.55 Å. Also, a π-alkyl interaction between the compound and the TRP86 residue for hydrophobic stability was seen. The **HM-5** exhibits a binding score of −8.1 kcal/mol. It forms many hydrogen bonds with TYR337 (2.90 Å), ASP74 (2.05 Å), TYR341 (3.06 Å), and HIS447 (2.20 Å), determining strong electrostatic interactions. The hydroxyl and methyl groups in the structure of **HM-5** make it possible to form hydrogen bonds and hydrophobic interactions in the catalytic cavity. A π and sigma interaction with TYR337 at 3.81 Å was found. Hydrophobic interactions were seen by means of a few π-alkyl interactions with TRP86. Although the binding scores of all the compounds were relatively low compared to galantamine, the interaction profiles of **HM-1** and **HM-5**. Overall, galantamine remained the most effective binder, while HM-1 (−8.6 kcal/mol) showed the highest binding energy among derivatives. Reduced scores in HM-2 and HM-4 likely reflect steric effects or suboptimal orientation, whereas extensive H-bonding and aromatic stabilization in HM-1 and

HM-5 indicate stable pocket accommodation, positioning HM-1 and HM-2 as promising candidates for further investigation as AChE inhibitors. Figure 9 shows the results for HM-1, HM-2, HM-5 and the reference remaining result is in S1 in supplementary. The favourable binding interactions observed for HM-1, HM-2, and HM-3 in the present docking analysis are consistent with their previously reported experimental AChE inhibitory activity (Li et al. 2023), supporting the biological relevance of the predicted binding modes.

Table 5: Docking results for galantamine and HM-1 to HM-5 against 4EY6.

Compounds	Residues	Distance	Type of interaction	Docking score
Reference	SER203	2.86	Conventional Hydrogen Bond	-10.4
	GLU202	2.76	Conventional Hydrogen Bond	
	SER203	3.77	Carbon Hydrogen Bond	
	HIS447	3.33	Carbon Hydrogen Bond	
	TYR124	3.33	Carbon Hydrogen Bond	
	SER125	3.61	Carbon Hydrogen Bond	
	TRP86	3.58	Pi-Sigma	
	GLY121, GLY122	3.94	Amide-Pi Stacked	
	TRP86	4.46	Pi-Alkyl	
	PHE295	4.27	Pi-Alkyl	
	PHE297	4.59	Pi-Alkyl	
	PHE338	4.89	Pi-Alkyl	
	HIS447	5.02	Pi-Alkyl	
HM-1	ASN87	2.47	Conventional Hydrogen Bond	-8.6
	HIS447	2.13	Conventional Hydrogen Bond	
	TRP86	3.87	Pi-Sigma	
	TRP86	4.74	Pi-Alkyl	
HM-2	TYR124	3.05	Conventional Hydrogen Bond	-8.0
	TYR337	2.89	Conventional Hydrogen Bond	
	TYR124	3.01	Carbon Hydrogen Bond	
	TRP86	3.52	Pi-Sigma	
	TYR341	3.93	Pi-Sigma	
	TRP86	5.49	Pi-Alkyl	
	TRP86	5.19	Pi-Alkyl	
	HIS447	5.00	Pi-Alkyl	
HM-3	TYR337	2.84	Conventional Hydrogen Bond	-8.3
	TYR341	3.25	Conventional Hydrogen Bond	
	TRP86	3.57	Pi-Sigma	

	TYR337	3.89	Pi-Sigma	
	TRP86	5.20	Pi-Alkyl	
	TRP86	4.61	Pi-Alkyl	
	HIS447	5.29	Pi-Alkyl	
HM-4	TYR337	2.96	Conventional Hydrogen Bond	-8.0
	ASP74	2.22	Conventional Hydrogen Bond	
	TRP86	3.82	Pi-Sigma	
	TYR337	3.45	Pi-Sigma	
	TRP86	3.55	Pi-Sigma	
	TRP86	4.68	Pi-Alkyl	
HM-5	TYR337	2.90	Conventional Hydrogen Bond	-8.1
	ASP74	2.05	Conventional Hydrogen Bond	
	TYR341	3.06	Conventional Hydrogen Bond	
	HIS447	2.19	Conventional Hydrogen Bond	
	TYR337	3.81	Pi-Sigma	
	TRP86	4.09	Pi-Alkyl	
	TRP86	4.93	Pi-Alkyl	
	TRP86	4.48	Pi-Alkyl	
	TRP86	3.87	Pi-Alkyl	
	HIS447	5.25	Pi-Alkyl	



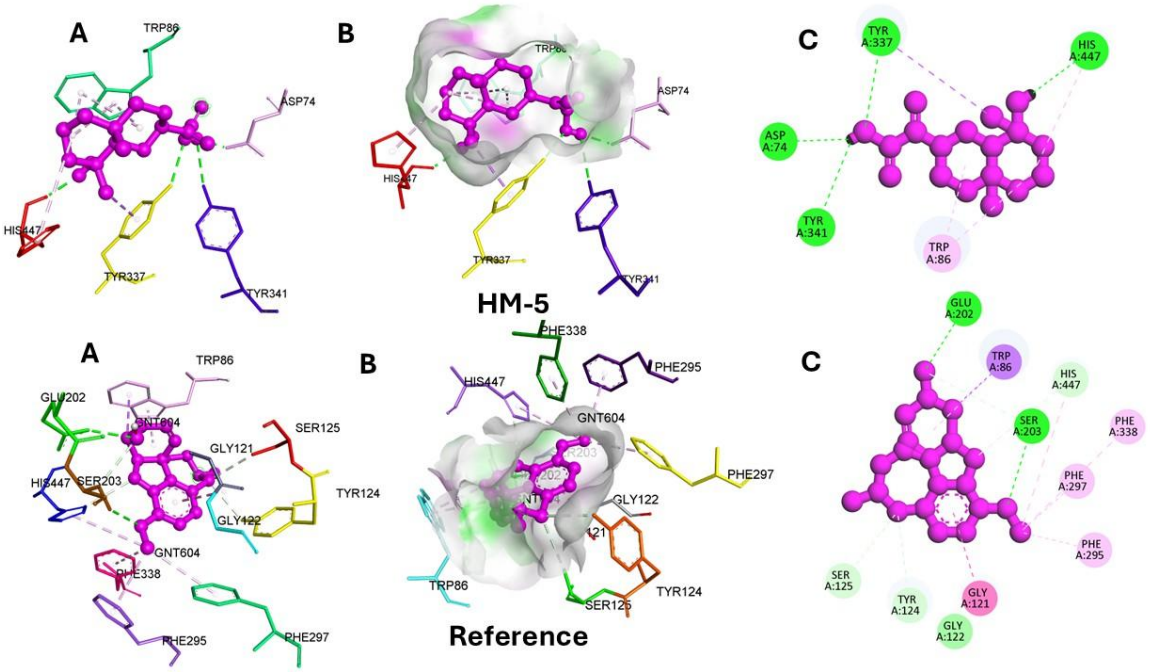


Fig 9 (A) 3D view of amino acid interaction (B) Hydrogen Bond interaction view (C) 2D amino acid interaction view of 4EY6 with HM-1, HM-2, HM-5 and R.

3.10. Molecular Dynamic simulation

The HM1 complex was evaluated over 300 ns by tracking backbone RMSD with respect to the minimized starting structure due to its better docking score and favorable toxicity profile. Following a rapid initial rise during the first ~10–15 ns, characteristics of early relaxation from the minimized geometry, the RMSD stabilized between 0.15 and 0.20 nm and was maintained until ~150 ns. A gradual shift subsequently stabilized the trajectory into a slightly higher, equally stable plateau of 0.20–0.23 nm for the remainder of the run, with only minor transient peaks (~0.26 nm) that relaxed within a few nanoseconds. This smooth, gradual transition between two stable phases rather than an abrupt or sustained excursion reflects a modest local conformational adjustment, most likely loop settling, and is uniform with overall structural stability rather than unfolding. Per-residue RMSF showed most residues fluctuating below 0.2 nm, reflecting a rigid core, with distinct flexible loops near residues 75–90, 220–290, and 480–500 (0.3–0.6 nm), consistent with surface-exposed regions of AChE as shown in figure 10. The N- and C-termini showed the highest fluctuations (~1.0 nm), a routine feature of unrestrained chain ends. Taken together, these results indicate that the catalytic core of AChE remained rigid and conformationally stable throughout the simulation, with flexibility localized to peripheral loops and terminal regions, supporting a well-maintained, suitable binding environment for **HM1**. Protein ligand hydrogen bond analysis showed **HM1** maintaining persistent polar

contact with AChE throughout the 300 ns simulation, primarily engaging 1–3 hydrogen bonds, with occasional peaks reaching 4. Complete loss of hydrogen bonding was rarely observed for the ligand, and the fluctuation between bonding states reflects normal dynamic behavior rather than gradual dissociation. This continuous, fluctuating profile supports a stable and favorable binding mode for **HM1** within the AChE active site. This stability is also supported by the radius of gyration, which, after a brief rise within the first ~20–40 ns, oscillated tightly between 2.30 and 2.335 nm for throughout the remainder of the trajectory as shown in figure 11. The absence of any net drift or expansion indicates that the enzyme's global compactness and tertiary packing was well retained throughout the simulation.

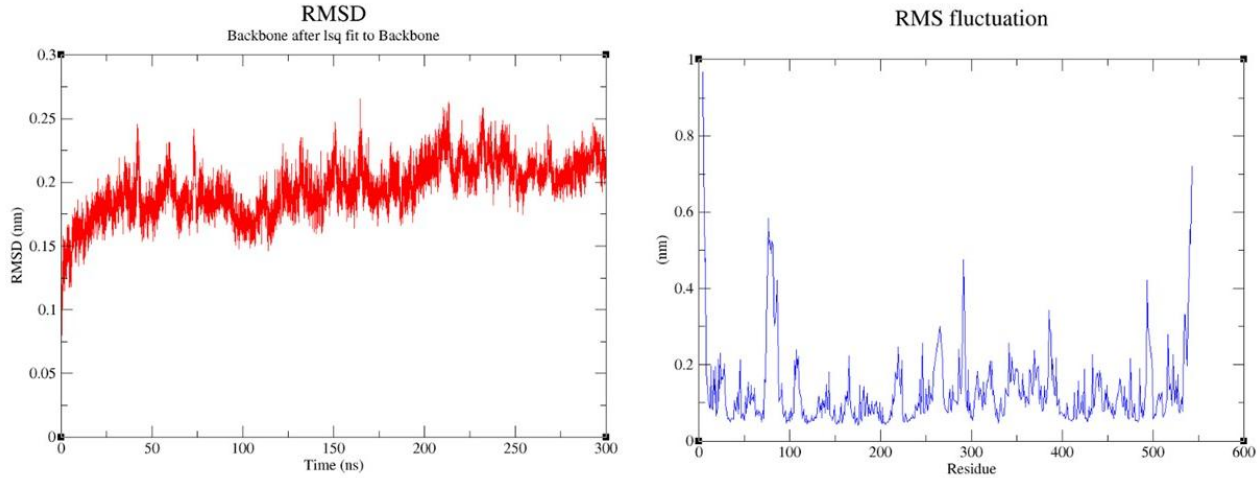


Fig 10: RMSD and RMS plot

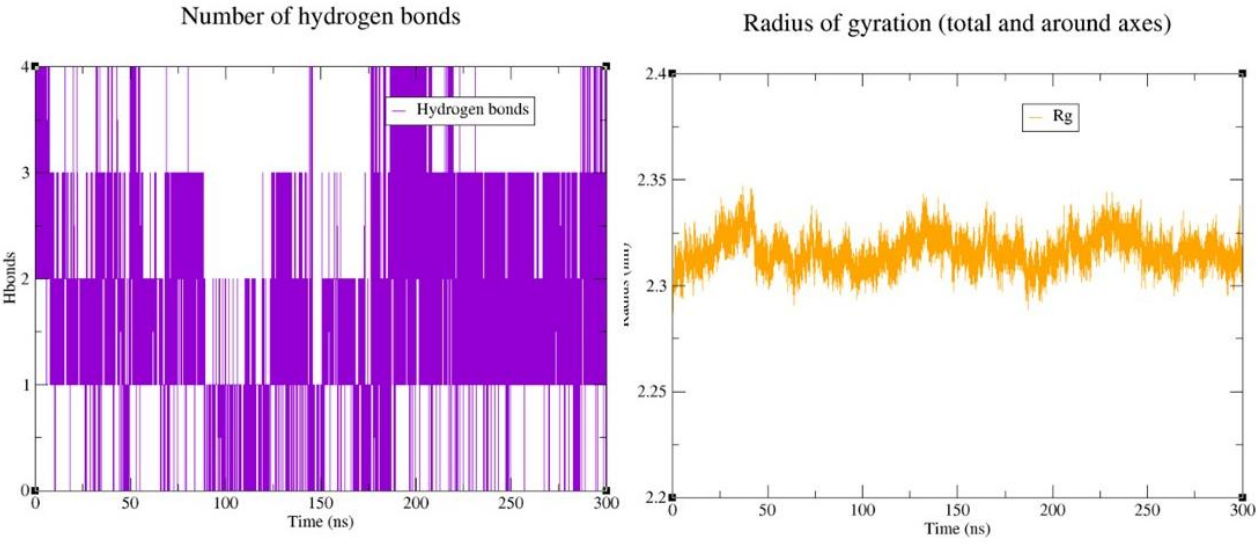


Fig:11 Radius of gyration and H-bond plots

3.11. MM/GBSA Calculation

Binding energies for the AChE-**HM1** complex were calculated from the steady segment of the 300 ns MD trajectory using the MM-GBSA method in gmx_MMPBSA. Entropic contributions

were not included, so the values are reported as enthalpic binding energies (ΔH) and are best used for relative comparison rather than as absolute binding free energies. Energy decomposition Table 6 shows that van der Waals interactions (ΔVDWAALS = −26.31 ± 0.31 kcal/mol) are the major favourable contribution, followed by gas-phase electrostatics (ΔEEL = −13.38 ± 0.52 kcal/mol). However, the polar solvation term (ΔGGB = +29.13 ± 0.40 kcal/mol) more than compensates the electrostatic gain, indicating the desolvation cost of burying polar groups at the binding interface. The nonpolar solvation term added a small favourable contribution (ΔGSA = −3.81 ± 0.04 kcal/mol). Together, these gave a gas-phase energy (ΔGGAS) of −39.68 ± 0.62 kcal/mol and a solvation energy (ΔGSOLV) of +25.32 ± 0.37 kcal/mol, for a total binding enthalpy of ΔH = −14.37 ± 0.38 kcal/mol. Binding was therefore driven mainly by van der Waals packing, with electrostatic gains offset by desolvation. MM/GBSA was performed only for the lead compound; comparison with the other candidates and the reference remains for future work.

Table :6 MM-GBSA binding energy and its energy components (kcal/mol) for the AChE-HM1complex

Energy Component	**ΔG (kcal/mol)**
ΔE_{vdw} (van der Waals)	-26.31 ± 0.31
ΔE_{elec} (Electrostatic)	-13.38 ± 0.52
ΔG_{gas} **(**$\Delta E_{\text{vdw}} + \Delta E_{\text{elec}}$**)**	-39.68 ± 0.62
ΔG_{GB} (Polar Solvation)	$+29.13 \pm 0.40$
ΔG_{SA} (Non-polar Solvation)	-3.81 ± 0.04
ΔG_{solv} **(**$\Delta G_{\text{GB}} + \Delta G_{\text{SA}}$**)**	$+25.32 \pm 0.37$
ΔH **(**$\Delta G_{\text{gas}} + \Delta G_{\text{solv}}$**)**	-14.37 ± 0.38

3.12. In Silico ADME Prediction

ADMETlab 3.0 was employed to predict the ADME properties of the reference compound and the natural products (**HM-1 to HM-5**) (Table 6). All six compounds were predicted to exhibit high human intestinal absorption, indicating favorable oral bioavailability potential across the entire series. Caco-2 permeability values for the natural products ranged from −4.6904 (**HM-2**) to −5.2742 (**HM-1**), all lower than the reference (−4.3126), while MDCK permeability values were more tightly clustered, ranging from −4.6192 (HM-2) to −4.8997 (**HM-5**), closely paralleling the reference (−4.6864). With respect to blood-brain barrier permeation, the reference compound and **HM-1** and **HM-5** were predicted to be BBB-permeant, whereas **HM-**

2, HM-3, and **HM-4** were predicted as non-permeant, indicating restricted central nervous system access for these three derivatives. PPB values were particularly higher among all natural products than the reference (21.32%), suggesting that the natural products have a higher degree of drug-protein bound state and a lower proportion of unbound drugs in their circulation in contrast to the reference. All six compounds, including the reference and natural compounds, were shown to be non-inhibitors for both CYP1A2 and CYP2D6 metabolism. Regarding CYP3A4 substrate behavior, only **HM-5** was predicted to act as a CYP3A4 substrate, while the reference and the remaining four natural products were predicted as non-substrates. Plasma clearance varied across the series, with **HM-4** (6.8455 mL/min/kg) and **HM-2** (6.2002 mL/min/kg) exceeding the reference (6.1759 mL/min/kg), while **HM-1** (3.4348), **HM-3** (2.7079), and **HM-5** (3.2296) showed comparatively lower clearance, with **HM-3** displaying the slowest clearance among the entire series.

Table 7. The ADME analysis for reference and HM-1 to HM-5

ADME Parameter	**Reference**	**HM-1**	**HM-2**	**HM-3**	**HM-4**	**HM-5**
Human Intestinal Abs. (HIA)	High	High	High	High	High	High
Caco-2 Permeability	-4.3126	-5.2742	-4.6904	-4.6925	-4.6937	-5.2431
MDCK Permeability	-4.6864	-4.8417	-4.6192	-4.7121	-4.8024	-4.8997
Blood-Brain Barrier (BBB)	Permeant	permeant	Non-Permeant	Non-permeant	Non-permeant	Permeant
Plasma Protein Binding (PPB)	21.32%	49.53%	50.56%	52.03%	64.77%	48.71%
CYP1A2 Inhibitor	Non-inhibitor	Non-inhibitor	Non-inhibitor	Non-inhibitor	Non-inhibitor	Non-inhibitor
sCYP2D6 Inhibitor	Non-inhibitor	Non-inhibitor	Non-inhibitor	Non-inhibitor	Non-inhibitor	Non-inhibitor

CYP3A4 Substrate	No	No	NO	No	No	yes
Clearance	6.1759	3.4348	6.2002	2.7079	6.8455	3.2296

3.13. Toxicity Prediction

In Table 7, the results of the toxicity prediction experiment benchmarked with the proposed reference and all compounds (**HM-1 to HM-5**) are displayed. The predicted organ toxicities and toxicity endpoints were evaluated and presented along with the corresponding probability values. With respect to hepatotoxicity, the reference compound was classified as inactive with a high probability (0.93), and this favourable profile was largely retained across the series, with **HM-1** (0.56), **HM-2** (0.68), **HM-4** (0.84), and **HM-5** (0.50) all predicted as inactive. **HM-3**, on the other hand, behaves differently, showing to be active with low probability (0.57), which suggests a moderate hepatotoxic potential. In neurotoxicity, the reference drug was predicted to be active (0.78). But particularly, most of the natural products investigated showed a safer toxicity profile in contrast to the reference, as **HM-1, HM-2, HM-4**, and **HM-5** were inactive (0.67, 0.67, 0.90, and 0.73, respectively). HM-3 was a single exception because it was active (0.66), showing similarity with the reference. In nephrotoxicity, the reference compound (0.81) and most natural compounds were inactive; these include **HM-1** (0.63), **HM-3** (0.75), **HM-4** (0.68), and **HM-5** (0.65). But **HM-2** stands alone showing activity but with a low probability value of (0.50), indicating a low nephrotoxicity profile. In respiratory toxicity, the reference compound (0.95) along with all five compounds remained active, with predicted values between 0.72 (**HM-2**) and 0.87 (**HM-1**), implying that this toxicity remained across all compounds regardless of structural alterations. In cardiotoxicity, the reference molecule was found inactive (0.82), but natural compounds were found to be active with low probability values. **HM-1** (0.64), **HM-2** (0.61), **HM-4** (0.54), **HM-5** (0.67), and **HM-3** (0.60) stand alone and remain as inactive as the reference. It suggests that many natural compounds exhibit slightly higher cardiotoxicity compared to the reference. At the end, in the immunotoxicity, the reference compound was active with very high probability (0.98). On the other hand, all the natural compounds displayed favourably. **HM-1** was active (0.91), while **HM-2** (0.95), **HM-3** (0.57), **HM-4** (0.77) and **HM-5** (0.67) were inactive. This suggests that the overall toxicity profile of natural extracts was better than the reference. They all show safer and more favourable toxicity ranges in contrast to the reference.

Table 8: Toxicity profile of HM-1 to HM-5 and Reference.

Toxicity Parameter	Reference	HM-1	HM-2	HM-3	HM-4	HM-5
Hepatotoxicity	Inactive (0.93)	Inactive (0.56)	Inactive (0.68)	Active (0.57)	Inactive (0.84)	Inactive (0.50)
Neurotoxicity	Active (0.78)	Inactive (0.67)	Inactive (0.67)	Active (0.66)	Inactive (0.90)	Inactive (0.73)
Nephrotoxicity	Inactive (0.81)	Inactive (0.63)	Active (0.50)	Inactive (0.75)	Inactive (0.68)	Inactive (0.65)
Respiratory toxicity	Active (0.95)	Active (0.87)	Active (0.72)	Active (0.74)	Active (0.74)	Active (0.85)
Cardiotoxicity	Inactive (0.82)	Active (0.64)	Active (0.61)	Inactive (0.60)	Active (0.54)	Active (0.67)
Immunotoxicity	Active (0.98)	Active (0.91)	Inactive (0.95)	Inactive (0.57)	Inactive (0.77)	Inactive (0.67)

4. Conclusion:

In this research, five (**05**) selected *sesquiterpenoids* found in *Laggera pterodonta*, namely, Laggeranine **A**, Laggeranine **B**, Pterodontic Acid, Pterodontriol **A**, and Ilicic Acid, designated as (**HM-1** to **HM-5**), were investigated in the context of Alzheimer's disease, using galantamine as a reference, which is a proven drug. Electronic properties of these natural compounds were studied using density functional theory; DFT was used to examine the extensive range of reactivity parameters, where Laggeranine A (**HM-1**) shows similar electronic properties to galantamine.**HM-1** and **HM-2** also show correlation with the experimental results, proving the reliability of this computational study. Additionally, Molecular docking shows that all five compounds occupy the active site of AChE and form favourable binding, also highlighting galantamine binding interactions via hydrogen bonds and π-interactions. All compounds displayed binding scores in the range of -8.0 to -8.6 Kcal/mol. The 300 ns molecular dynamics simulation demonstrated that the receptor-HM1 complex shows acceptable conformationally stable, with stable backbone RMSD and radius of gyration, localized flexibility in peripheral loops, and persistent protein-ligand hydrogen-bonding interactions. MM/GBSA analysis yielded a favourable binding enthalpy of −14.37 ± 0.38 kcal/mol, primarily driven by van der Waals interactions, further supporting the stability of **HM1** within the AChE binding site. The most significant findings are that the ADMET analysis showed that Laggeranine A and Ilicic Acid (**HM-1** and **HM-5**) cross the blood-brain barrier; however, all five natural extracts have

shown comparably safer and more favourable profiles for the body than galantamine in neurotoxicity and immunotoxicity profiles. The predicted binding modes of HM-1, HM-2, and HM-3 further align with previously reported experimental AChE inhibitory activity, supporting their potential as AChE-targeting candidates. In summary, these findings show that the *Laggera pterodonta* extracts have great importance as natural candidates along with galantamine, with some of the molecules having similar neuroprotective impacts to galantamine and some even being computational safer and more favourable.

Acknowledgements

This work was supported and funded by the Deanship of Scientific Research at Imam Mohammad Ibn Saud Islamic University (IMSIU) (grant number IMSIU-DDRSP2601).

Author contributions

Conceptualization Hamza Iftikhar, Muhammad Mohsin Ejaz, ; **original draft writing and editing:** Hamza Iftikhar, Muhammad Mohsin Ejaz and Sadaf Ashraf, Reviewing Saira Khan**,** Nazia Meer, and Musarat Riaz **Formal analysis, Funding acquisition** K.S. Al-Namshah, Muhammad Saleem, **Resources:** Saira Khan **Data validation, data curation:** Muhammad Saleem.

Funding

Authors are thankful to the Higher Education Commission (HEC) for the NRPU Research Grant No. 15788.

Conflict of interest

The authors declare no competing interests.

Data availability

The data presented in the current study will be available on demand.

Ethical approval

Not applicable.

Statement of human and animal rights

Not applicable.

Statement of informed consent

Not applicable.

References

Abdelaziz B, Chérif I, Gassoumi B, Patanè S, Ayachi S (2023) Linear and Nonlinear Optical Responses of Nitrobenzofurazan-Sulfide Derivatives: DFT-QTAIM Investigation on Twisted Intramolecular Charge Transfer. The Journal of Physical Chemistry A 127:9895-9910. 10.1021/acs.jpca.3c04277

Abraham M, Alekseenko, A., Andrews, B., Basov, V., Bauer, P., Bird, H., Briand, E., Brown, A., Doijade, M., Fiorin, G., Fleischmann, S., Gorelov, S., Gouaillardet, G., Gray, A., Irrgang, M. E., Jalalypour, F., Johansson, P., Kutzner, C., Łazarski, G., ... Lindahl, E. (2025) GROMACS 2025.4 Manual (Version 2025.4). Zenodo https://doi.org/10.5281/zenodo.17671776

Abraham MJ, Murtola T, Schulz R et al (2015) GROMACS: High performance molecular simulations through multi-level parallelism from laptops to supercomputers. SoftwareX 1-2:19-25. https://doi.org/10.1016/j.softx.2015.06.001

Akman F, Kutlu Br (2025) Quantum Chemical Calculations, Topological Properties, ADME/Molecular Docking Studies, and Hirshfeld Surface Analysis on Some Organic UV-Filters. ACS Omega 10:14884-14907. 10.1021/acsomega.4c10102

Allal H, Nemdili H, Zerizer MA, Zouchoune B (2024) Molecular structures, chemical descriptors, and pancreatic lipase (1LPB) inhibition by natural products: a DFT investigation and molecular docking prediction. Structural Chemistry 35:223-239. 10.1007/s11224-023-02176-2

AmeliMojarad M, AmeliMojarad M (2024) The neuroinflammatory role of microglia in Alzheimer's disease and their associated therapeutic targets. CNS Neuroscience & Therapeutics 30:e14856. 10.1111/cns.14856

Bakheit AH, Wani TA, Al-Majed AA et al (2024) Theoretical study of the antioxidant mechanism and structure-activity relationships of 1,3,4-oxadiazol-2-ylthieno[2,3-d]pyrimidin-4-amine derivatives: a computational approach. Frontiers in Chemistry Volume 12 - 2024:10.3389/fchem.2024.1443718

Banerjee P, Kemmler E, Dunkel M, Preissner R (2024) ProTox 3.0: a webserver for the prediction of toxicity of chemicals. Nucleic Acids Res 52:W513-w520. 10.1093/nar/gkae303

Barukial P, Nandi R, Ahmed M et al (2026) Computational insights into Ru(ii)–coumarin complexes as potential anticancer agents: a DFT, QTAIM, NCI-RDG, molecular docking and molecular dynamics approach. Physical Chemistry Chemical Physics 28:1447-1462. 10.1039/d5cp03171k

Behl C (2023) Focus on neurochemistry led to the cholinergic hypothesis of Alzheimer's disease. In: Alzheimer's disease research: what has guided research so far and why it is high time for a paradigm shift. Springer, pp 73-91

Bekker H, Berendsen HJ, Dijkstra E et al Gromacs-a parallel computer for molecular-dynamics simulations. In: 4th international conference on computational physics (PC 92), 1993. World Scientific Publishing, pp 252-256

Belghalia E, Elbamtari F, Bouamrane S et al (2026) Integrated computational evaluation of flavonoids from Artemisia campestris L. as FLT3 inhibitors: molecular docking, dynamics, ADMET, DFT, and topological (ELF, LOL) insights. Journal of Molecular Modeling 32:207. 10.1007/s00894-026-06785-6

BIOVIA (2025) Discovery Studio Visualizer. Dassault Systèmes, San Diego, CA

Boudjahem I, Nemamcha A, Moumeni H, Brahimi N (2025) Study of heteroatom-doped graphene properties using DFT/TD-DFT, QTAIM, NBO, and NCI calculations. Structural Chemistry 36:947-974. 10.1007/s11224-024-02427-w

Brooks BR, Brooks III CL, Mackerell Jr. AD et al (2009) CHARMM: The biomolecular simulation program. Journal of Computational Chemistry 30:1545-1614. https://doi.org/10.1002/jcc.21287

Chaudhary T, Chaudhary MK, Joshi BD (2021) Topological and reactivity descriptor of carisoprodol from DFT and molecular docking approach. Journal of Institute of Science and Technology 26:74-82.

Chen Z-R, Huang J-B, Yang S-L, Hong F-F (2022) Role of Cholinergic Signaling in Alzheimer's Disease. Molecules 27:1816.

Cheung J, Rudolph MJ, Burshteyn F et al (2012) Structures of human acetylcholinesterase in complex with pharmacologically important ligands. Journal of medicinal chemistry 55:10282-10286. 10.1021/jm300871x

Dhifet M, Guelmami L, Zaki K et al (2025) Comprehensive synthesis and characterization of a novel Fe–porphyrin complex: crystal structure, spectroscopic investigations, Hirshfeld surface analysis, and computational modeling (DFT, QTAIM-NCI/ELF). Frontiers in Chemistry Volume 13 - 2025:10.3389/fchem.2025.1666671

Fu L, Shi S, Yi J et al (2024) ADMETlab 3.0: an updated comprehensive online ADMET prediction platform enhanced with broader coverage, improved performance, API functionality and decision support. Nucleic Acids Res 52:W422-w431. 10.1093/nar/gkae236

Gajendra K, Pratap GK, Poornima DV, Shantaram M, Ranjita G (2024) Natural acetylcholinesterase inhibitors: A multi-targeted therapeutic potential in Alzheimer's disease. European Journal of Medicinal Chemistry Reports 11:100154. https://doi.org/10.1016/j.ejmcr.2024.100154

Garbuz DG, Zatsepina OG, Evgen'ev MB (2021) Beta Amyloid, Tau Protein, and Neuroinflammation: An Attempt to Integrate Different Hypotheses of Alzheimer's Disease Pathogenesis. Molecular Biology 55:670-682. 10.1134/S002689332104004X

Gaussian 09 RD, M. J. Frisch, G. W. Trucks, H. B. Schlegel, G. E. Scuseria, M. A. Robb, J. R. Cheeseman, G. Scalmani, V. Barone, G. A. Petersson, H. Nakatsuji, X. Li, M. Caricato, A. Marenich, J. Bloino, B. G. Janesko, R. Gomperts, B. Mennucci, H. P. Hratchian, J. V. Ortiz, A. F. Izmaylov, J. L. Sonnenberg, D. Williams-Young, F. Ding, F. Lipparini, F. Egidi, J. Goings, B. Peng, A. Petrone, T. Henderson, D. Ranasinghe, V. G. Zakrzewski, J. Gao, N. Rega, G. Zheng, W. Liang, M. Hada, M. Ehara, K. Toyota, R. Fukuda, J. Hasegawa, M. Ishida, T. Nakajima, Y. Honda, O. Kitao, H. Nakai, T. Vreven, K. Throssell, J. A. Montgomery, Jr., J. E. Peralta, F. Ogliaro, M. Bearpark, J. J. Heyd, E. Brothers, K. N. Kudin, V. N. Staroverov, T. Keith, R. Kobayashi, J. Normand, K. Raghavachari, A. Rendell, J. C. Burant, S. S. Iyengar, J. Tomasi, M. Cossi, J. M. Millam, M. Klene, C. Adamo, R. Cammi, J. W. Ochterski, R. L. Martin, K. Morokuma, O. Farkas, J. B. Foresman, and D. J. Fox. (2016). Gaussian, Inc, Wallingford CT

Getahun T, Sharma V, Gupta N (2019) The genus Laggera (Asteraceae) – Ethnobotanical and Ethnopharmacological Information, Chemical Composition as well as Biological Activities of Its Essential Oils and Extracts: A Review. Chemistry & Biodiversity 16:e1900131. 10.1002/cbdv.201900131

Gustavsson A, Norton N, Fast T et al (2023) Global estimates on the number of persons across the Alzheimer's disease continuum. Alzheimer's & Dementia 19:658-670. 10.1002/alz.12694

H Ferreira-Vieira T, M Guimaraes I, R Silva F, M Ribeiro F (2016) Alzheimer's disease: targeting the cholinergic system. Current neuropharmacology 14:101-115.

Humphrey W, Dalke A, Schulten K (1996) VMD: Visual molecular dynamics. Journal of Molecular Graphics 14:33-38. https://doi.org/10.1016/0263-7855(96)00018-5

Hussein HA, Fadhil GF (2023) Theoretical Investigation of para Amino-Dichloro Chalcone Isomers. Part II: A DFT Structure–Stability Study of the FMO and NLO Properties. ACS Omega 8:4937-4953. 10.1021/acsomega.2c07148

Kalola UK, Patel P, Nguyen H (2026) Galantamine. StatPearls Publishing, Treasure Island (FL),

Kochman U, Sitka H, Kuźniar J et al (2025) Targeted Nanoparticles for Drug Delivery Across the Blood–Brain Barrier in Early and Late Stages of Alzheimer's Disease: A Review. Molecular Neurobiology 63:75. 10.1007/s12035-025-05417-z

Koirala M, Karimzadegan V, Liyanage NS, Mérindol N, Desgagné-Penix I (2022) Biotechnological Approaches to Optimize the Production of Amaryllidaceae Alkaloids. Biomolecules 12:10.3390/biom12070893

Lee J, Cheng X, Swails JM et al (2015) CHARMM-GUI Input Generator for NAMD, GROMACS, AMBER, OpenMM, and CHARMM/OpenMM Simulations Using the CHARMM36 Additive Force Field. Journal of Chemical Theory and Computation 12:405-413. 10.1021/acs.jctc.5b00935

Li J, Li F, Wu G et al (2023) Acetylcholinesterase inhibitory activity of sesquiterpenoids isolated from Laggera pterodonta. Frontiers in Plant Science Volume 14 - 2023:10.3389/fpls.2023.1074184

Lu T (2024) A comprehensive electron wavefunction analysis toolbox for chemists, Multiwfn. The Journal of Chemical Physics 161:10.1063/5.0216272

Ma C, Hong F, Yang S (2022) Amyloidosis in Alzheimer's Disease: Pathogeny, Etiology, and Related Therapeutic Directions. Molecules 27:1210.

Martins MM, Branco PS, Ferreira LM (2023) Enhancing the Therapeutic Effect in Alzheimer's Disease Drugs: The role of Polypharmacology and Cholinesterase inhibitors. ChemistrySelect 8:e202300461. 10.1002/slct.202300461

Muya JT, Mwanangombo DT, Tsalu PV et al (2019) Conceptual DFT study of the chemical reactivity of four natural products with anti-sickling activity. SN Applied Sciences 1:1457. 10.1007/s42452-019-1438-8

Nasb M, Tao W, Chen N (2024) Alzheimer's disease puzzle: delving into pathogenesis hypotheses. Aging and disease 15:43.

Nguyen DB, Cárdenas C, Lira J et al (2025) The electron localization function and the chemical interpretation of Fermi orbital descriptors in Fermi–Löwdin self-interaction correction calculations. The Journal of Chemical Physics 162:10.1063/5.0263003

Pardo-Moreno T, González-Acedo A, Rivas-Domínguez A et al (2022) Therapeutic Approach to Alzheimer's Disease: Current Treatments and New Perspectives. Pharmaceutics 14:1117.

Rajesh SM, Kumar DCV, Shalini V et al (2025) Structural analysis and computational studies of cyclopropane derivative as an anti- Alzheimer's agent: Investigation of interactions by X-ray crystallography, DFT, molecular docking, and ADMET approaches. Journal of Molecular Structure 1341:142665. 10.1016/j.molstruc.2025.142665

Rashid EU, Hadia NMA, Shawky AM et al (2023) Quantum modeling of dimethoxyl-indaceno dithiophene based acceptors for the development of semiconducting acceptors with outstanding photovoltaic potential. RSC advances 13:4641-4655. 10.1039/d2ra07957g

Rawat P, Sehar U, Bisht J et al (2022) Phosphorylated Tau in Alzheimer's Disease and Other Tauopathies. International Journal of Molecular Sciences 23:12841.

Schrodinger, LLC (2015) The PyMOL Molecular Graphics System, Version 1.8.

Silva LB, Ferreira EFB, Maryam et al (2023) Galantamine Based Novel Acetylcholinesterase Enzyme Inhibitors: A Molecular Modeling Design Approach. Molecules 28:1035.

Sumathi S, Karthik N, Jeyavijayan S (2025) Computational and Spectroscopic Insights Into 4-Methoxychalcone as a Potential Acetylcholinesterase Inhibitor: A DFT and Molecular Docking Approach. International Journal of Quantum Chemistry 125:e70092. 10.1002/qua.70092

Taşpınar N, Bulduk İ (2022) Alternative Analytical Methods for Quantification of Galantamine in Pharmaceuticals. Ege Tıp Bilimleri Dergisi 5:58-64. 10.33713/egetbd.1161168

Thakor VS, Tyagi A, Lee Jr JM et al (2024) Alois Alzheimer (1864-1915): The Father of Modern Dementia Research and the Discovery of Alzheimer's Disease. Cureus 16:

Tiéba TN, Charles KK, Stéphane DG et al (2023) Theoretical Study of Reactivity and Stability of a Thiazine Derivative Series by the Density Functional Theory (DFT) Method. Journal of Materials 11:1-7.

Trott O, Olson AJ (2010) AutoDock Vina: Improving the speed and accuracy of docking with a new scoring function, efficient optimization, and multithreading. Journal of Computational Chemistry 31:455-461. 10.1002/jcc.21334

Valdés-Tresanco MS, Valdés-Tresanco ME, Valiente PA, Moreno E (2021) gmx_MMPBSA: A New Tool to Perform End-State Free Energy Calculations with GROMACS. Journal of Chemical Theory and Computation 17:6281-6291. 10.1021/acs.jctc.1c00645

Yan Y-P, Chen J-Y, Lu J-H (2022) Disease-Modifying Activity of Huperzine A on Alzheimer's Disease: Evidence from Preclinical Studies on Rodent Models. International Journal of Molecular Sciences 23:15238.

Zhang J, Zhang Y, Wang J et al (2024) Recent advances in Alzheimer's disease: Mechanisms, clinical trials and new drug development strategies. Signal transduction and targeted therapy 9:211.

Supplementary Files

This is a list of supplementary files associated with this preprint. Click to download.

- Supplementarymaterial1.docx